*nanomaterials*

MDPI

*Article*

# A Theoretical Study of the Occupied and Unoccupied Electronic Structure of High- and Intermediate-Spin Transition Metal Phthalocyaninato (Pc) Complexes: VPc, CrPc, MnPc, and FePc

**Silvia Carlotto [1,2,*], Mauro Sambi [1], Francesco Sedona [1], Andrea Vittadini [2] and Maurizio Casarin [1,2,*]**

[1] Dipartimento di Scienze Chimiche, Università degli Studi di Padova, via F. Marzolo 1, 35131 Padova, Italy; mauro.sambi@unipd.it (M.S.); francesco.sedona@unipd.it (F.S.)
[2] Istituto di Chimica della Materia Condensata e di Tecnologie per l'Energia (ICMATE-CNR), via F. Marzolo 1, 35131 Padova, Italy; andrea.vittadini@unipd.it
* Correspondence: silvia.carlotto@unipd.it (S.C.); maurizio.casarin@unipd.it (M.C.)

**Abstract:** The structural, electronic, and spectroscopic properties of high- and intermediate-spin transition metal phthalocyaninato complexes (MPc; M = V, Cr, Mn and Fe) have been theoretically investigated to look into the origin, symmetry and strength of the M–Pc bonding. DFT calculations coupled to the Ziegler's extended transition state method and to an advanced charge density and bond order analysis allowed us to assess that the M–Pc bonding is dominated by $\sigma$ interactions, with FePc having the strongest and most covalent M–Pc bond. According to experimental evidence, the lightest MPcs (VPc and CrPc) have a high-spin ground state (GS), while the MnPc and FePc GS spin is intermediate. Insights into the MPc unoccupied electronic structure have been gained by modelling M $L_{2,3}$-edges X-ray absorption spectroscopy data from the literature through the exploitation of the current Density Functional Theory variant of the Restricted Open-Shell Configuration Interaction Singles (DFT/ROCIS) method. Besides the overall agreement between theory and experiment, the DFT/ROCIS results indicate that spectral features lying at the lowest excitation energies (*EE*s) are systematically generated by electronic states having the same GS spin multiplicity and involving M-based single electronic excitations; just as systematically, the $L_3$-edge higher *EE* region of all the MPcs herein considered includes electronic states generated by metal-to-ligand-charge-transfer transitions involving the lowest-lying $\pi^*$ orbital ($7e_g$) of the phthalocyaninato ligand.

**Keywords:** transition metal phthalocyaninato complexes; X-ray absorption spectroscopy (XAS); Density Functional Theory (DFT); Restricted Open-Shell Configuration Interaction Singles (ROCIS)



**Citation:** Carlotto, S.; Sambi, M.; Sedona, F.; Vittadini, A.; Casarin, M. A Theoretical Study of the Occupied and Unoccupied Electronic Structure of High- and Intermediate-Spin Transition Metal Phthalocyaninato (Pc) Complexes: VPc, CrPc, MnPc, and FePc. *Nanomaterials* **2021**, *11*, 54. https://doi.org/10.3390/nano11010054

Received: 10 November 2020
Accepted: 22 December 2020
Published: 28 December 2020



## 1. Introduction

Phthalocyanines ($H_2Pc$) share with porphyrins ($H_2P$), everywhere present "as far as the living world is concerned" [1], the same four nitrogen-based coordinative pockets. Even though $H_2Pc$ and its metal complexes (MPc) are not present in Nature, they have been attracting great interdisciplinary interest because their technological potential spans over a wide range of applications [2,3]. Besides traditional appliances, such as dyestuffs for textiles and inks [3], MPcs are currently used as intrinsic semiconductors, chemical sensors, organic light-emitting diodes, organic photovoltaic cells, thin-film transistors, materials for nonlinear optics, spintronics and laser recording [4–8]. Moreover, bio-inspired oxygen-binding MPcs have been shown as viable substitutes for precious metals in catalysts for the oxygen reduction reaction (ORR) in low-temperature fuel cells [9–12]. As intimate an understanding as possible of the origin, symmetry, and strength of the M–Pc interaction is then mandatory to enhance the efficiency of new MPc-based devices. As such, X-ray absorption spectroscopy (XAS) is unanimously recognized as a valuable tool to probe, element-selectively, the empty electronic structure of M complexes, the M coordinative environment, as well as the nature and the strength of the M–ligand interaction [13–16].

Metal $L_{2,3}$-edges' spectral features are related to the electronic states generated by the electric dipole-allowed 2p → *n*d excitations [17], thus providing information about the contribution of the M-based *n*d atomic orbitals (AOs) to the frontier virtual molecular orbitals (VMOs). Metal-based $2p^6 \ldots nd^k \rightarrow 2p^5 \ldots nd^{k+1}$ excitations create a hole in the M 2p core AOs with an angular momentum quantum number $\ell = 1$, and spin-orbit coupling (SOC) allows $\vec{\ell}$ to couple with $\vec{s}$, whose quantum number $s = 1/2$. Two distinct states are then produced ($j = 3/2$ and $j = 1/2$), with the former (the $L_3$-edge) lying at lower excitation energy (*EE*) and having an intensity approximately twice that of the $L_2$-edge associated with $j = 1/2$. Besides the M $L_{2,3}$-edges, the ligand (L) donor atom K-edge XA spectra of ML complexes with partly filled *n*d AOs are usually characterized by rather intense pre-edge features. These are associated with the electronic states generated by the electric dipole-allowed L-based 1s → *m*p transitions [17], whose intensity gauges the L *m*p character of frontier VMOs [18–21]. XAS at the L K-edge thus directly probes the so-called M−L symmetry-restricted covalency [22], affording information complementary to that gatherable by XAS at the M $L_{2,3}$-edges. Despite the fact that the $L_{2,3}$-edges spectra of ML complexes contain a huge amount of chemical information, their first-principle modelling is theoretically demanding because, besides the ligand field and covalency effects, SOC between the possible many final-state multiplets has to be considered [23–32].

At the very beginning of this century, Koshino et al. [33] recorded the $L_{2,3}$ excitation spectra of MPc ($24 \leq Z \leq 29$; Z corresponds to the atomic number of the metals they considered) by exploiting the inner-shell electron energy-loss spectroscopy (ISEELS); a little over ten years later, Kroll et al. [34] investigated the electronic structure of MPc ($25 \leq Z \leq 30$) by combining soft L-edge XAS and 2p photoemission spectroscopy. In addition, few years ago, Eguchi et al. [35] succeeded in the ultra-high vacuum synthesis and XAS characterization of VPc on Ag(111), while neither XAS nor ISEELS data have been so far reported for TiPc to our knowledge.

As a part of a systematic investigation of the electronic properties of energy-targeted materials, some of us have recently investigated their structure/reactivity relationships by exploiting XAS at the N K-edge and at the M $L_{2,3}$-edges of diverse MPc (M = V [36,37], Fe [12,38] and Cu [37,39,40]) and CuTPP/CuTPP(F) [41] ($H_2$TPP = tetraphenylporphyrin; $H_2$TPP(F) = tetrakispentafluorophenyl porphyrin) surface-supported films coupled to quantum mechanical calculations. Two different methodologies were adopted to model the M $L_{2,3}$-edges' features: the current Density Functional Theory variant of the Restricted Open-Shell Configuration Interaction Singles (DFT/ROCIS) method [42] (VPc, FePc and CuPc) and the Relativistic Time-Dependent DFT (RTD-DFT), including SOC with full use of symmetry and correlation effects [43] within the Tamm−Dancoff approximation [44] (CuPc, CuTPP, CuTPP(F)). As such, it has to be noted that, besides L donor atom K-edge XA spectra of ML complexes [39,41,45–47], the RTD-DFT approach may be employed to satisfactorily models the M $L_{2,3}$-edges XAS features of closed shell [46,48] and $Cu^{II}$ complexes. Indeed, the modelling of the $Cu^{II}$ $L_{2,3}$-edges features corresponds, among open shell complexes, to the simplest possible case because the electric dipole allowed $2p^6 \ldots 3d^9 \rightarrow 2p^5 \ldots 3d^{10}$ transitions generate a final configuration, which has only two term symbols. The corresponding spectral splitting is dominated by the 2p SOC contribution and the overall energetics and intensities are strongly influenced by ligand-field and covalency, respectively [40]. At variance to that, the RTD-DFT approach is unable to suitably describe SOC in open-shell molecules as explicitly reported in the ADF manual. All the MPcs herein considered (M = V, Cr, Mn and Fe) are open-shell systems with a quite complex electronic structure. A RTD-DFT modelling of their XAS features would then be utterly inadequate, while they can be properly handled by exploiting the module ROCIS of the ORCA program package [42].

In this contribution, a homogeneous modelling of the VPc, CrPc, MnPc, and FePc $L_{2,3}$-edges' features is presented and discussed with the ultimate goal of providing a first-principle rationale of differences characterizing the M–Pc interaction along the investigated series. As such, it can be useful to mention that, with the exception of VPc,

recently synthesized in extreme conditions [35], the remaining MPcs herein considered all have relevant catalytic applications, including the: (i) CO and NO oxidation as well as ORR (CrPc) [49–52]; (ii) oxidation reactions in homogeneous and heterogeneous phase (MnPc) [9]; (iii) N-alkylation [53], C–H amination [54], C–C bond formation [55], synthesis of esters [56] and oximes [57] as well as reduction [58], oxidation [59,60], and radical reactions (FePc) [61]. Moreover, bio-inspired oxygen-binding Fe-macrocycles are particularly appealing as a consequence of their ability to reversibly bind $O_2$, a crucial step in processes such as respiration, photosynthesis or the ORR catalysis [62]. Thus, there is no doubt that a comprehension as intimate as possible of the M–Pc interaction is of paramount importance to design new MPc-like species devoted to specific purposes.

## 2. Computational Details

The ground state (GS) electronic and structural properties of title molecules have been herein investigated by exploiting the Amsterdam Density Functional (ADF) package [63] within the assumption of an idealized $D_{4h}$ symmetry [17] (see Figure 1), by running spin-unrestricted, nonrelativistic DFT calculations, with generalized gradient corrections self-consistently included through the Becke−Perdew formula [64,65], by adopting a triple-$\zeta$ with a polarization function Slater-type basis set for all the atoms, and by freezing the M 1s–2p AOs and the 1s AO of N and C atoms throughout the calculations. MPc optimized Cartesian coordinates are reported in Tables S1–S4 of the Supplementary Materials.

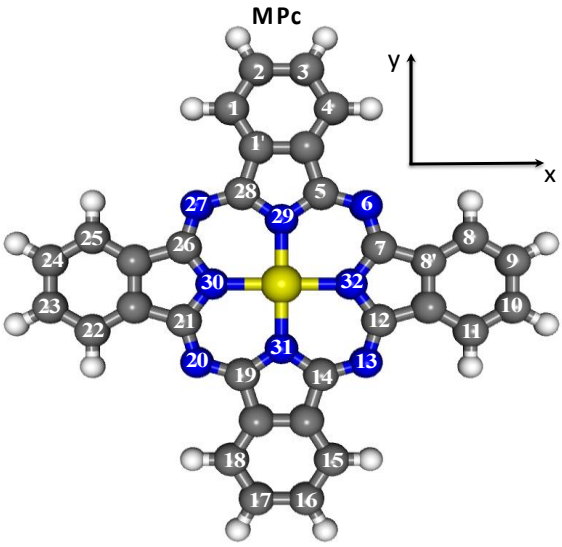


**Figure 1.** Schematic representation of a $D_{4h}$ MPc molecule with the atom numbering recommended by the International Union of Pure and Applied Chemistry (IUPAC). White, grey, blue and yellow spheres correspond to H, C, N, and M atoms, respectively. In the adopted framework, the molecular $\sigma_h$ plane corresponds to the xy plane. N(29), N(30), N(31) and N(32) (N(6), N(13), N(20) and N(27)) are collectively labelled $N^{Py}$ ($N^{m}$).

Insights into the origin, symmetry, and strength of the M–Pc interaction have been gained by combining the Nalewajski−Mrozek approach [66–71], well suited to estimating bond multiplicity indices ($^{NM}$I) in M complexes [66–72], with the Ziegler's extended transition state (ETS) method [73]. According to the ETS scheme, the MPc bonding energy (*BE*) may be written as:

$$BE = -(\Delta E_{es} + \Delta E_{Pauli} + \Delta E_{orb}) \quad (1)$$

where $\Delta E_{es}$ accounts for the pure electrostatic interaction, $\Delta E_{Pauli}$ represents the destabilizing two-orbital−four-electrons interaction between the occupied orbitals of the interacting fragments (only atomic fragments have been herein considered), and $\Delta E_{orb}$ corresponds

to the stabilizing interaction between the occupied and empty orbitals of the atomic fragments. In passing, $\Delta E_{orb}$ may be further decomposed into contributions due to the different irreducible representations (IRs) of the $D_{4h}$ point group, according to

$$\Delta E_{orb} = \sum_{\chi} \Delta E_{orb}^{\chi}, \quad (2)$$

The MPc $L_{2,3}$-edges' XA spectra [33–35] have been modelled by evaluating *EE*s and corresponding oscillator strength distributions ($f(EE)$) for transitions with the M 2p-based MOs as initial spin orbitals (*isos*), by means of the DFT/ROCIS method [30], which includes SOC in a molecular Russell−Saunders fashion [25], by adopting the B3LYP exchange–correlation (XC) functional [74] for VPc, CrPc and FePc and the M06 meta-GGA XC [75] for MnPc (vide infra), and by using the def2-TZVP(-f) basis set [76,77]. The combined use of DFT and configuration interaction requires a set of three semi-empirical parameters ($c_1$ = 0.18, $c_2$ = 0.20, and $c_3$ = 0.40), which have been calibrated by Roemelt and Neese [25] for a test set of M $L_{2,3}$-edges. Throughout the M $L_{2,3}$-edges modelling, the resolution of identity approximation has been used with the def-TZVP/J basis set [76,77]. Moreover, the zero-th order regular approximation has been adopted to treat the scalar relativistic effects [78]. Numerical integrations for DFT/ROCIS calculations have been carried out on a dense Lebedev grid (302 points) [79]. In addition, MPc-modelled spectra have been shifted by 10.9 (VPc), 9.8 (CrPc), 8.3 (MnPc) and 13.1 (FePc) eV to superimpose the highest intensity features of the simulated and experimental $L_3$-edge, which does not suffer from the extra broadening and the distortion due to the Coster–Kronig Auger decay process [32,80]. This was needed because absolute theoretical *EE*s carry errors arising from DF deficiencies in the core region, one-particle-basis set restrictions and inadequacies in the modelling of spin-free relativistic effects [24].

## 3. Results and Discussion

### *3.1. MPc Occupied Electronic Structure*

The aim of obtaining an understanding as intimate as possible of the origin, symmetry and strength of the M–Pc interaction may benefit from a preliminary, qualitative description of the MPc frontier orbitals simply based on symmetry arguments and overlap considerations. MPcs are united by the presence of the $Pc^{2-}$ ligand whose electronic properties have been thoroughly described elsewhere [81]. $Pc^{2-}$ frontier MOs may be split into $\sigma$ and $\pi$ sets. MPc symmetry adapted linear combinations (SALC) of C and N $2p_\sigma$ (C and N $2p_\pi$) are bases for the following $D_{4h}$ IRs: $a_{1g}$, $a_{2g}$, $b_{1g}$, $b_{2g}$, $e_u$ ($e_g$, $a_{1u}$, $a_{2u}$, $b_{1u}$, $b_{2u}$); moreover, among $\pi$ MOs, no $a_{1u}$ SALC of N $2p_\pi$ AOs, no $b_{1u}$ SALC of $N^{Py}$ $2p_\pi$ AOs and no $b_{2u}$ SALC of $N^{m}$ $2p_\pi$ AOs (see Figure 1) is present. In addition, the four $N^{Py}$ lone pairs pointing toward the centre of the coordinative pocket are bases for the $a_{1g}$, $b_{1g}$ and $e_u$ IRs. In more detail, the two $Pc^{2-}$ highest occupied MOs (HOMOs) correspond to the $15b_{1g}$ MO, $\sigma$ in character and strongly localized on the $N^{Py}$ lone pairs pointing toward the centre of the coordinative pocket, and the $2a_{1u}$ $\pi$ MO. In this regard, it is noteworthy that the $D_{4h}$ $a_{1u}$ IR is anti-symmetric with respect to the reflections through the $\sigma_h$, $\sigma_v$ and $\sigma_d$ symmetry planes of the $D_{4h}$ point group; the $a_{1u}$ $\pi$ MOs have then a node on symmetry planes passing through $N^{Py}$ and $N^{m}$ atoms (see Figure 1). As far as the $D_{4h}$ $Pc^{2-}$ lowest unoccupied MO (LUMO) is concerned, the $6e_g$ VMO has a $\pi$ character too.

The presence of the $Pc^{2-}$ square planar ligand field lifts the five-fold degeneracy of the M 3d AOs, generating a $3d_\sigma$ and a $3d_\pi$ set. The former set includes the $21a_{1g}$ ($z^2$-based) and the $16b_{1g}$ ($x^2$–$y^2$-based) MOs, while the latter takes in the $14b_{2g}$ (xy-based) and the $6e_g$ (xz- and yz-based) ones [17]. Among them, the $21a_{1g}$ and the $14b_{2g}$ MOs are substantially M–$N^{Py}$ non-bonding, while the $6e_g$ and $16b_{1g}$ MOs are M–$N^{Py}$ $\pi$ and $\sigma$ antibonding, respectively. Relative energy positions of the $3d_\sigma/3d_\pi$ spin up (↑)/spin down (↓) sets in VPc, CrPc, MnPc and FePc are displayed in Figure 2, together with those of selected Pc-based MOs.

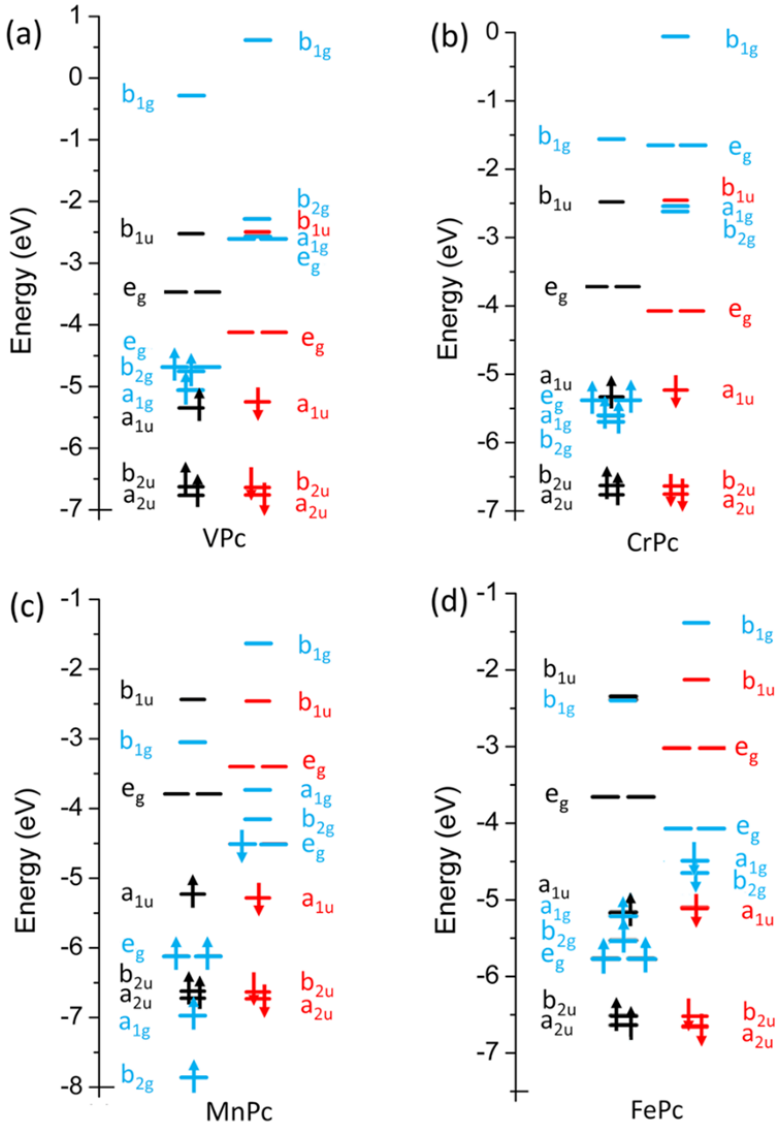


**Figure 2.** Relative energy positions of VPc (**a**), CrPc (**b**), MnPc (**c**) and FePc (**d**) frontier MOs. Black (↑)/red (↓) arrows refer to Pc-based selected orbitals, while the blue ones correspond to the M 3d-based MOs.

*VPc ground state*. Experimental [35] and theoretical [36,37,82] results disagree about the VPc ground state (GS) spin multiplicity. Carlotto et al. [36,37] recently proposed a $^4E_g$ high-spin (HS) GS ($a_{1g}^1\ b_{2g}^1\ e_g^1\ b_{1g}^0$; see Figure 2 and Table 1; possible Jahn–Teller distortions [83] associated with orbitally degenerate GS or excited states have not been taken into account), while Eguchi et al. [35] presumed a $^2E_g$ low-spin (LS) GS ($a_{1g}^0\ b_{2g}^2\ e_g^1\ b_{1g}^0$). The $^2$Eg state generated by the $a_{1g}^0 b_{2g}^2 e_g^1 b_{1g}^0$ configuration is 52.1 (35.5) kcal/mol less stable than the HS $^4E_g$ (LS $^2B_{1g}$) one; moreover, the $^4B_{1g}/^4A_{2g}$ states generated by the constrained $a_{1g}^0 b_{2g}^1 e_g^2 b_{1g}^0 / a_{1g}^1 b_{2g}^0 e_g^2 b_{1g}^0$ configurations are 1.8/1.7 kcal/mol less stable than the $^4$Eg GS. Consistently with the VPc $a_{1g}^1\ b_{2g}^1\ e_g^1\ b_{1g}^0$ GS configuration, the $^{NM}I_{V\text{-}N}{}^{Py}$ is quite large (0.64) [36]; as such, since $^{NM}$I includes both covalent and ionic contributions, it is of some relevance to mention that the V Hirshfeld [84] charge ($Q_V$) amounts to 0.34.

A closer look at the frontier VPc GS electronic structure indicates that all the V 3d-based singly occupied MOs (SOMOs) lie well above the ring-based, V-free, $2a_{1u}$ $\pi$ doubly occupied MO (DOMO). The ionization energies (*IE*s) of VPc frontier MOs are not available in the literature; nevertheless, their values may be estimated by exploiting the Slater

transition state (TS) method [85], which allows the evaluation of excitation/ionization energies " ... by means of an artificial state that is halfway between the ground state of an atom or molecule and an excited state" [86]. Interestingly, the lowest VPc TS*IE* (6.17 eV) is associated with the ionization from the V $3d_{\pi}$-based $6eg^{\uparrow}$ SOMO rather than with the photoemission from the ring-based, V-free, $2a_{1u}$ $\pi$ DOMO (6.59 eV). In this regard, it is of value to highlight that in his seminal paper devoted to the investigation of gas-phase photoelectron (PE) spectra of $H_2Pc$ and MPc (M = Mg, Fe, Co, Ni, Cu, and Zn), J. Berkowitz pointed out that " ... the first ionization potential occurs at ~6.4 eV, and it varies almost imperceptibly from sample to sample, including metal free and MgPc. Therefore, the conclusion seems inescapable that the first ionization potential corresponds to electron ejection from a ring orbital, and not a metal orbital" [87].

**Table 1.** BP86 $\Delta BE$ (kcal/mol) of optimized $D_{4h}$ VPc, CrPc, MnPc and FePc with different spin states. GSs are taken as reference.

| S | VPc | CrPc | MnPc | FePc |
|---|---|---|---|---|
| 0 | | NC [a] | | 31.9 ($^1A_{1g}$) [b] |
| 1/2 | 16.6 ($^2B_{1g}$) | | 14.9 ($^2B_{2u}$) | |
| 1 | | 25.6[b] ($^3E_u$) | | 0 ($^3A_{2g}$)[90] |
| 3/2 | 0 ($^4E_g$) | | 0 ($^4E_g$) | |
| 2 | | 0 ($^5B_{1g}$) | | NC[a] |
| 5/2 | | | 16.5 ($^6E_g$) | |

[a] NC stands for non-converged; [b] Non-Aufbau.

The comparison of the VPc bond lengths and bond angles with those optimized for the other MPc (see Table 2) [88] indicates that the structural perturbations induced by the presence of different $M^{II}$ ions in the $Pc^{2-}$ coordinative pocket are rather minute.

*CrPc ground state*. As already mentioned, CrPc has been attracting great interest as a catalyst for the CO and NO oxidation, as well as for the ORR [49–52], thus making particularly interesting the study of its electronic structure. $Cr^{II}$ has a $3d^4$ configuration, which may generate three spin states with S = 0 (LS), S = 1 (intermediate spin; IS) and S = 2 (HS). Any attempt to optimize the LS state failed (NC, non-converged in Table 1), while the $^3E_u$ IS state, associated with the $a_{1g}^1 b_{2g}^1 e_g^2 b_{1g}^0 2a_{1u}^{0\uparrow} / a_{1g}^0 b_{2g}^0 e_g^1 b_{1g}^0 2a_{1u}^{1\downarrow}$ configuration, has been found less stable than the $^5B_{1g}$ HS one, generated by the $a_{1g}^1 b_{2g}^1 e_g^2 b_{1g}^0$ configuration, by 25.6 kcal/mol (IS and HS CrPc optimized structures are perfectly superimposable). Incidentally, the $^3E_u$ IS state implied a non-Aufbau occupation accompanied by a pseudo reduction (oxidation) of the $Cr^{II}$ ion (macrocycle). As such, even though the $^5B_{1g}$ HS GS has been experimentally revealed [89,90] and theoretically predicted [36,82], the localization of VMOs is still controversial. Indeed, SIESTA [91] numerical experiments carried out by Arillo-Flores et al. [82] are consistent with the absence of " ... metal contributions to HOMO and LUMO, they principally localize upon the inner ring.", which is certainly correct for the M-free $2a_{1u}$ HOMO, but wrong for the $6e_g^{\downarrow}$ LUMO. In addition, differently from VPc, the ring-based, Cr-free, the $2a_{1u}$ $\pi$ DOMO corresponds to the CrPc HOMO (see Figure 2). Analogously to VPc, the *IE*s of the CrPc frontier MOs are not available in the literature, but, differently from VPc, the lowest TS*IE* value (6.60 eV) is estimated for the ionization from the ring-based, Cr-free, $2a_{1u}$ $\pi$ HOMO.

**Table 2.** Theoretical and experimental [88] (in parentheses) structural parameters for $D_{4h}$ VPc, CrPc, MnPc and FePc. Bond lengths/bond angles in Å/°, respectively.

| | $M–N^{Py}$ | $N^{Py}–C$ | $N^{m}–C$ | $M–N^{Py}–C$ | $N^{Py}–C–N^{m}$ |
|---|---|---|---|---|---|
| VPc * | 1.996 | 1.392 | 1.333 | 125.4 | 127.4 |
| CrPc * | 1.982 | 1.387 | 1.330 | 125.6 | 127.5 |
| MnPc [a] | 1.952 (1.938) | 1.396 (1.392) | 1.324 (1.315) | 126.1 (126.2) | 127.4 (127.6) |
| FePc [b] | 1.935 (1.927) | 1.393 (1.378) | 1.321 (1.322) | 126.4 (126.3) | 127.3 (127.8) |

* Neither VPc nor CrPc crystallographic data are available in the literature; [a] from Ref. [92]; [b] from Ref. [93].

Upon moving from VPc to CrPc, the GS frontier electronic configuration evolves from $a_{1g}^1 b_{2g}^1 e_g^1 b_{1g}^0$ to $a_{1g}^1 b_{2g}^1 e_g^2 b_{1g}^0$. The addition of an electron to the $3d_\pi$-based $6e_g{}^\uparrow$ MO, $M–N^{Py}$ anti-bonding could then be invoked to rationalize the ${}^{NM}I_{M\text{-}N}{}^{Py}$ reduction from 0.64 (see above) to 0.43. Nevertheless, three things need to be kept in mind before drawing conclusions: (i) as already mentioned, ${}^{NM}I$ includes both covalent and ionic contributions; (ii) $Q_{Cr}$ (0.49) is larger than $Q_V$ (0.34); (iii) the $3d_\pi$-based $6e_g{}^\uparrow$ MO is more anti-bonding in CrPc than in VPc (the localization % of the VPc $6e_g{}^\uparrow$ MO on $N^{Py}$ is negligible; see Figure 3).

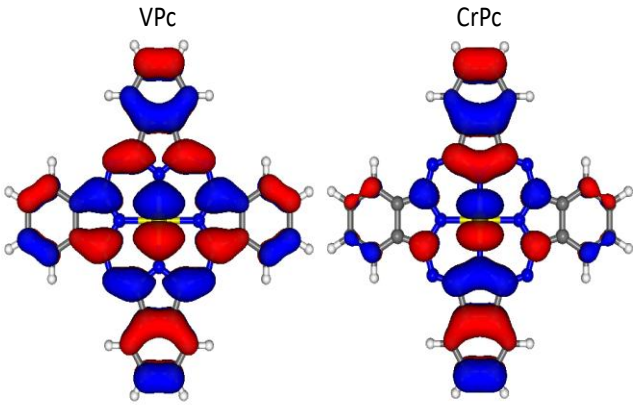


**Figure 3.** Three-dimensional plots of the VPc and CrPc $6e_g{}^\uparrow$ MO. Displayed isosurfaces correspond to $\pm$ 0.015 $e^{1/2}A^{-3/2}$.

Analogously to VPc, no crystallographic data are available in the literature for CrPc; nevertheless, the tiny differences between the CrPc- and VPc-optimized structural parameters seem to indicate that a subtle balance between ionic and anti-bonding covalent contributions to the M–Pc interaction, both of them larger in CrPc than in VPc, takes place.

*MnPc ground state*. Likewise CrPc, LS, IS and HS states are possible; moreover, even though the optimized structural parameters corresponding to different spin states are very similar, the ${}^4E_g$ IS state associated to the $a_{1g}^1 b_{2g}^1 e_g^3 b_{1g}^0$ configuration (see Figure 2) has been found more stable than the ${}^6E_g$ HS and the ${}^2B_{2u}$ LS ones by 16.5 and 14.9 kcal/mol, respectively. As such, it has to be noted that: (i) the MnPc IS GS has been experimentally [94–99] and theoretically [36,100–105] assessed; (ii) the ${}^6E_g$ HS state is generated by the $a_{1g}^1 b_{2g}^1 e_g^2 b_{1g}^0 7e_g^1$ configuration; (iii) the ${}^2B_{2u}$ LS state has the following occupation numbers: $a_{1g}^1 b_{2g}^1 e_g^2 b_{1g}^0 2a_{1u}^0{}^\uparrow / a_{1g}^0 b_{2g}^0 e_g^2 b_{1g}^0 2a_{1u}^1{}^\downarrow$. In this contest, it is noteworthy that: (i) both the $7e_g$ and the $2a_{1u}$ MOs are ring-based $\pi$ orbitals, so that the HS (LS) state would imply a pseudo $Mn^{II}$ oxidation (reduction) with the Mn 3d-based orbitals occupied by four (six) electrons (${}^{HS}Q_{Mn}$, ${}^{IS}Q_{Mn}$ and ${}^{LS}Q_{Mn}$ amount to 0.41, 0.33 and 0.28, respectively); (ii) to our knowledge, only two contributions [33,106] suggested a MnPc HS state. As regards the MnPc IS GS, a further controversy concerns its symmetry, or, equivalently, the occupation

numbers of the Mn 3d-based $21a_{1g}$, $14b_{2g}$ and $6e_g$ MOs. Three different configurations may be considered: $a_{1g}^1 b_{2g}^1 e_g^3 b_{1g}^0$ ($^4E_g$), $a_{1g}^1 b_{2g}^2 e_g^2 b_{1g}^0$ ($^4A_{2g}$) and $a_{1g}^2 b_{2g}^1 e_g^2 b_{1g}^0$ ($^4B_{1g}$). In agreement with the theoretical results of Brumboiu et al. [105], the ADF outcomes rule out the $^4B_{1g}$ state because of its high energy; moreover, it is noteworthy that different experimental studies support either a $^4E_g$ or a $^4A_{2g}$ GS. Specifically, XAS evidence [98], magnetic circular dichroism (MCD)/UV-Vis results [95], and XAS/MCD outcomes [99] favour a $^4E_g$ GS [107], while magnetic susceptibility measurements have been rationalized within the assumption of a $^4A_{2g}$ GS [95,97], which has been attributed to intermolecular interactions in the MnPc crystal. In agreement with the literature [101], the ADF results herein reported estimate the $^4E_g$ state to be more stable than the $^4A_{2g}$ by 7.3 kcal/mol.

Before going on, it is of some relevance to point out that the MnPc $a_{1g}^1 b_{2g}^1 e_g^3 b_{1g}^0$ GS configuration implies the presence of a high-lying Mn $3d_\pi$-based SOMO$^\downarrow$ well above the ring-based, Mn-free, $2a_{1u}$ $\pi$ DOMO (see Figure 2). As such, no gas-phase photoemission results are available in the literature for MnPc; however, Grobosch et al. [108] were able to record the He(I) photoemission spectrum of an MnPc thin film deposited on polycrystalline Au. Interestingly, they assigned the lowest lying peak of the MnPc valence band photoemission spectrum to the ionization from the Mn $3d_\pi$-based $6e_g^\downarrow$ MO, observing also that the $\Delta IE$ between the ring-based, Mn-free, $\pi$ $2a_{1u}$ DOMO and the $3d_\pi$-based $6e_g^\downarrow$ orbital is ~0.5 eV [108,109]. In perfect agreement with these findings [108], the TS*IE*s [85] of the highest-lying $6e_g^\downarrow$ and $2a_{1u}^\downarrow$ orbitals are 5.99 and 6.51 eV, respectively.

Among the investigated molecules, MnPc is the lightest one for which structural parameters are available [88,92]. The data reported in Table 2 reveal that optimized bond lengths and bond angles fairly reproduce experimental evidence. In this context, the $^{NM}I_{Mn\text{-}N}{}^{Py}$ value (0.52), just in between the $^{NM}I_{Cr\text{-}N}{}^{Py}$ and the $^{NM}I_{V\text{-}N}{}^{Py}$ ones (0.43 and 0.64, respectively), seems to indicate that the M–$N^{Py}$ bond-weakening associated with the addition of a further electron to the $3d_\pi$-based $6e_g$ MO is negligible (see Figure S1 of the Supplementary Materials). In addition, it has to be underlined that $Q_{Mn}$ (0.33) and $Q_V$ (0.34) are almost identical.

*FePc ground state.* Similarly to MnPc, experimental [34,110–114] and theoretical [38,104,115] evidence indicates a FePc IS GS whose symmetry is, however, still debated. On the computational side, the IS GS symmetry, inextricably linked to the occupation numbers of frontier MOs, has been found to be extremely sensitive to the adopted XC functional and basis set. Carlotto et al. [38] have proposed a $^3E_g$ IS GS, generated by a $a_{1g}^1 b_{1g}^2 e_g^3 b_{2g}^0$ configuration, on the basis of numerical experiments carried out by employing the ORCA program package [42], by using the hybrid B3LYP XC–functional [74], by adopting the def2-TZVP(-f) basis set [76,77] and the $c_1$, $c_2$, and $c_3$ semi-empirical parameters 0.21, 0.49, and 0.29 (hereafter, old set), respectively. In passing, the $a_{1g}^1 b_{1g}^2 e_g^3 b_{2g}^0$ GS configuration is a consequence of the orientation of the molecule in the xy plane. The x and y axes of the framework they adopted point toward the $N^m$ atoms rather than toward the $N^{Py}$ ones (see Figure 1). The four $N^{Py}$ lone pairs were then bases for the $a_{1g}$, $b_{2g}$ and $e_u$ IRs rather than for the $a_{1g}$, $b_{1g}$ and $e_u$ ones, and the Fe 3d-based VMO accounting for the Fe-$N^{Py}$ $\sigma$ anti-bonding interaction corresponded to the $14b_{2g}$ level rather than to the $16b_{1g}$ one. All the possible configurations compatible with a FePc IS GS have been herein considered. As such, even though the ADF $^3B_{2g}$ ($a_{1g}^1 b_{2g}^1 e_g^4 b_{1g}^0$) and the $^3E_g$ ($a_{1g}^1 b_{2g}^2 e_g^3 b_{1g}^0$) IS states are less stable than the $^3A_{2g}$ one ($a_{1g}^2 b_{2g}^2 e_g^2 b_{1g}^0$) by minute amounts (1.4 and 1.1 kcal/mol, respectively), it is of some relevance to underline that the $\Delta E_{orb}^{\chi}$ ($\chi$ = $a_{1g}$, $b_{2g}$ and $e_g$) of the IS states differ by up to ~230 kcal/mol ($\Delta E_{orb}^{e_g}$ = −2584.4, −2810.4 and −2690.4 kcal/mol in the $^3A_{2g}$, $^3B_{2g}$ and $^3E_g$ states, respectively). A further ADF $^3E_g$ state may be generated by the $a_{1g}^2 b_{2g}^1 e_g^3 b_{1g}^0$ configuration. Besides the non-Aufbau filling of the corresponding electronic levels, the latter $^3E_g$ state is significantly less stable than the $^3A_{2g}$ GS (12.3 kcal/mol). Additional numerical experiments have been carried out to estimate the FePc *BE* of the LS and HS states. As far as the former is concerned, it may imply either the $a_{1g}^0 b_{2g}^2 e_g^4 b_{1g}^0$ configuration or the $a_{1g}^2 b_{2g}^0 e_g^4 b_{1g}^0$ one. The LS $a_{1g}^2 b_{2g}^0 e_g^4 b_{1g}^0$ frozen configuration generates a non-Aufbau energy level filling, and a *BE*

lower (~32 kcal/mol) than that of the $^3A_{2g}$ GS; any attempt to get a converged *BE* value for the LS $a_{1g}^2 b_{2g}^0 e_g^4 b_{1g}^0$ frozen configuration failed. Analogous considerations hold for the HS state.

FePc is the lightest MPc for which gas-phase photoemission spectroscopy data have been recorded [87]. According to experimental evidence, the TS*IE* of the ring-based, Fe-free, $\pi$ $2a_{1u}$ DOMO is the lowest one. Incidentally, its value (6.51 eV) is very close to the one (6.49 eV) estimated by Liao and Scheiner [101], even though a non-relativistic approach has been herein adopted.

According to the experiment in Ref. [93], the shortening of the M–$N^{Py}$ distance upon moving from MnPc to FePc is correctly reproduced (see Table 2). In this context, it is of relevance to mention that $Q_{Fe}$ = 0.13; i.e., the smallest value along the investigated series. Such a result, coupled to the $^{NM}I_{Fe\text{-}N}{}^{Py}$ = 0.64, ultimately indicates that the Fe–$N^{Py}$ interaction is the most covalent among the molecules we took into account (look at the MPc $\Delta E_{orb}$ values reported in Table 3). In addition, the presence of a strong Fe–$N^{Py}$ covalent $\sigma$ interaction is consistent with the high-energy position of the $16b_{1g}{}^{\uparrow}$ VMO (see Figure 2), which accounts for the $\sigma$ anti-bonding interaction between the Fe $3d_{x^2\text{-}y^2}$ AO and the $b_{1g}$ SALC of the $N^{Py}$ lone pairs.

**Table 3.** BP86 $\Delta E_{orb}^{\chi}$ (kcal/mol) of GS $D_{4h}$ MPc herein considered (FePc is taken as a reference).

| | VPc | CrPc | MnPc | FePc |
|---|---|---|---|---|
| $a_{1g}$ | 100.9 | 106.7 | 103.8 | 0.0 |
| $b_{1g}$ | −86.8 | −85.9 | −26.8 | 0.0 |
| $b_{2g}$ | 81.6 | 99.6 | 86.2 | 0.0 |
| $e_g$ | −16.7 | −55.0 | −153.9 | 0.0 |
| $\Delta E_{orb}$ | 79.0 | 64.8 | 9.3 | 0.0 |

### *3.2. MPc Unoccupied Electronic Structure*

The MPc $L_{2,3}$-edges' XA spectra [33–35,38] herein modelled have been collected from deposits of different thicknesses, often consisting of randomly oriented and weakly interacting molecules. Thus, according to a procedure successfully tested in the past [36–41,116–120], XAS outcomes have been rationalized by completely neglecting the adsorbate/substrate interactions. Now, before moving to the modelling of the MPc XAS features, a few words about the $2p \rightarrow 3d$ excitations simply based on symmetry arguments may be useful to facilitate the forthcoming discussion. In a simplified picture of the $2p \rightarrow 3d$ one-electron excitations, the $M^{II}$ electronic configuration moves from the starting $\ldots$ $2p^6$ $\ldots$ $3d^k$ to the ending $\ldots$ $2p^5$ $\ldots$ $3d^{k+1}$ with $3 \leq k \leq 6$ for $23 \leq Z \leq 26$. The electronic states associated to the $\ldots$ $2p^5$ $\ldots$ $3d^{k+1}$ configurations, straightforwardly obtained by evaluating the $^2P \otimes D^{k+1}$ direct products (the whole set of multiplets arising from a particular $3d^{k+1}$ configuration is herein collectively labelled $D^{k+1}$) [121], are collected in Tables S5–S7 of the Supplementary Materials. The ligand-field, covalent interactions and SOC admixture further split them, to generate totals of $6 \times 210 = 1260$ (k + 1 = 4), $6 \times 252 = 1512$ (k + 1 = 5), $6 \times 210 = 1260$ (k + 1 = 6), and $6 \times 120 = 720$ (k + 1 = 7) molecular magnetic spin sublevels, respectively. The $M^{II}$ electronic configurations of the MPc herein considered (HS $V^{II}$ $a_{1g}^1 b_{2g}^1 e_g^1 b_{1g}^0$, HS $Cr^{II}$ $a_{1g}^1 b_{2g}^1 e_g^2 b_{1g}^0$, IS $Mn^{II}$ $a_{1g}^1 b_{2g}^1 e_g^3 b_{1g}^0$, IS $Fe^{II}$ $a_{1g}^2 b_{2g}^2 e_g^2 b_{1g}^0$) allow us to foresee that the one-electron excitation patterns describing the $M^{II}$ final states in the $D_{4h}$ symmetry should in principle include states having a spin multiplicity either equal to ($\Delta S = 0$) or lower/higher than ($\Delta S = \pm 1$) the GS. The $\Delta S = 0$ spin-selection rule is slightly released when SOC is considered; more specifically, SOC connects the terms with resultant spins S and S′, where $|S - S'| = 0, 1$ [122].

Electric dipole-allowed transitions imply that [17]

$$\Gamma_{GS} \otimes \Gamma_{\mu} \otimes \Gamma_{ES} \supset \Gamma_{Sym}, \quad (3)$$

where $\Gamma_{GS}$, $\Gamma_{\mu}$, $\Gamma_{ES}$ and $\Gamma_{Sym}$ correspond to the IRs of the MPc electronic GS, the dipole moment operator ($a_{2u}$ + $e_u$) [17], the electronic excited state ($\Gamma_{ES} = \Gamma_{iso} \otimes \Gamma_{GS} \otimes \Gamma_{fso}$; *iso*

and *fso* stand for initial and final spin orbitals, respectively), and the totally symmetric representation of the $D_{4h}$ point group ($a_{1g}$), respectively. Equation (3) may then evolve to

$$\Gamma_{iso} \otimes (a_{2u} + e_u) \otimes \Gamma_{fso} \supset a_{1g}, \quad (4)$$

which implies that, within the adopted approximation, which reduces the complete one-electron excited configuration space (1h–1p space) to the subspace where only the M 2p core electrons (transforming as $a_{2u} + e_u$) [17] are excited, the allowed electric dipole transitions are

$$(a_{2u} \rightarrow a_{1g})^{\perp} \quad (5)$$

$$(a_{2u} \rightarrow e_g)^{||} \quad (6)$$

$$(e_u \rightarrow e_g)^{\perp} \quad (7)$$

$$(e_u \rightarrow a_{1g}/a_{2g}/b_{1g}/b_{2g})^{||} \quad (8)$$

where the $||/\perp$ symbols stand for parallel/perpendicular to the molecular $\sigma_h$ plane (see Figure 1).

*VPc $L_3$-edge.* To date, only Eguchi et al. have succeeded in synthesizing, even though in extreme conditions, surface-supported mono- and multi-layers of VPc, whose angle-dependent linearly polarized XA spectra at the V $L_{2,3}$-edges are reported in Ref. [35]. As such, a thorough analysis of the $||$ and $\perp$ V $L_{2,3}$-edges components of the VPc and OVPc XA spectra has been recently reported by Carlotto et al. [36,37]. With specific reference to the VPc complex, the authors were able to conclusively assess its spin state by modelling corresponding XAS features for both LS (S = 1/2) and HS (S = 3/2) states. A brief description of their HS results [36] is herein included to favour the comparison with the modelled spectra of diverse MPcs.

It has been already mentioned that the one-electron excitation pattern describing the $V^{II}$ final states in $D_{4h}$ symmetry should be dominated by states which may have (see Table S5 of the Supporting Materials) either a spin multiplicity equal to ($\Delta S = 0$) or lower/higher ($\Delta S = \pm 1$) than the GS one [122]. As such, it has to be underlined that the ORCA B3LYP HS GS corresponds to the $^4A_{2g}$ state generated by the $a_{1g}^1 b_{2g}^0 e_g^2 b_{1g}^0$ electronic configuration. B3LYP/ROCIS outcomes [36,37] indicate that both the $^{||}f(EE)$ and the $^{\perp}f(EE)$ distributions of the $L_3$-edge mainly arise from states having $\Delta S = 0$, while $\Delta S = \pm 1$ contributions are negligible. Moreover, the lowest-lying $^{||/\perp}L_3{}^1$ features (see Figure 4a) are due to states generated by V 2p → SOMOs single electronic excitations. Incidentally, SOMOs correspond to the V 3d-based $6e_g$ and $21a_{1g}$ orbitals, while states associated to coupled-single electronic excitations [25,32], mainly involving V 2p → SOMOs and SOMOs → VMOs excitations, contribute to $^{||/\perp}L_3{}^2$. SOMOs naturally correspond to the $21a_{1g}$ and $6e_g$ MOs, while the VMOs are the V 3d-based $14b_{2g}$ (~90%) and the $\pi^*$ Pc-based $7e_g$ (~10%) orbitals. In passing, the MPc $7e_g$ VMO corresponds to the lowest-lying Pc-based $\pi^*$ orbital and metal-to-ligand-charge-transfer (MLCT) transitions in diverse MPc $L_3$-edge spectra (vide infra) involve this VMO. No contribution from V 2p → $16b_{1g}$ excitations is provided to states associated with the VPc $L_3$-edge.

The agreement between the experimental evidence and B3LYP/ROCIS outcomes has been documented in detail elsewhere [36,37]; here, it is sufficient to underline that both the relative positions and relative intensities of spectral features are well reproduced by $^{||/\perp}f(EE)$. Major disagreements between theory and experiment usually affect the $L_2$ region [31]; nonetheless, it deserves mentioning that the B3LYP/ROCIS $^{||}L_2{}^1$–$^{||}L_3{}^{2\,HS}\Delta EE$ (6.4 eV, see Figure 4a) fairly reproduces the experimental value (6.9 eV). Any further comment about the VPc $L_2$-edge is herein avoided.

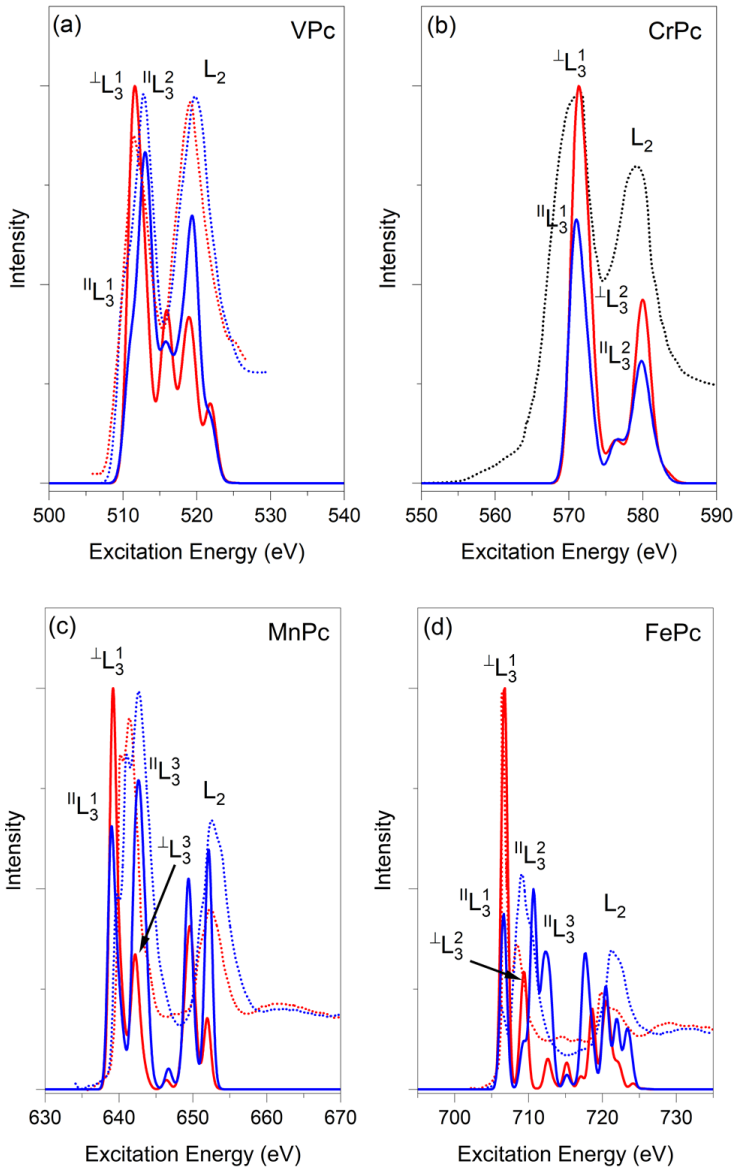


**Figure 4.** Experimental (dotted lines) and calculated (solid lines) $^{\parallel/\perp}f(EE)$ distributions for $^{HS}$VPc (**a**), $^{HS}$CrPc (**b**), $^{IS}$MnPc (**c**) and $^{IS}$FePc (**d**). Blue and red lines correspond to $\parallel$ and $\perp$ components, respectively. Simulated spectra have been shifted by 10.9 ($^{HS}$VPc), 9.8 ($^{HS}$CrPc), 8.3 ($^{IS}$MnPc) and 13.1 ($^{IS}$FePc) eV and have a Gaussian broadening of 1.8 ($^{HS}$VPc), 2.0 ($^{HS}$CrPc), 1.0 ($^{IS}$MnPc) and 1.0 ($^{IS}$FePc) eV. Only the total experimental spectrum (black dotted line) is available for CrPc [33]; MnPc $^{\parallel/\perp}f(EE)$ distributions have been obtained by using the hybrid M06 meta-GGA XC [75] (see text).

*CrPc $L_3$-edge.* To date, the only CrPc $f(EE)$ distribution for the 2p excitations is the one recorded by Koshino et al. by exploiting ISEELS [33]. Their spectrum includes both the $L_3$- and the $L_2$-edge, but the coarse *EE* scale they adopted prevents the possibility of revealing the presence of possible structures associated to them; moreover, no information is provided by the authors about the $L_2$–$L_3$ $\Delta EE$. Similarly to VPc, the one-electron excitation pattern describing the Cr final states in the CrPc $D_{4h}$ symmetry is dominated by states which may have (see Table S6 of the Supporting Material) a spin multiplicity either equal to ($\Delta S = 0$) or lower/higher ($\Delta S = \pm 1$) than the GS one. The HS CrPc $^{\parallel}f(EE)$ and $^{\perp}f(EE)$ B3LYP/ROCIS distributions are superimposed upon the CrPc ISEEL spectrum in Figure 4b. In the $L_3$-edge region, $^{\parallel/\perp}f(EE)$ consists of an intense peak ($L_3{}^1$) with an evident shoulder on its higher *EE*s ($L_3{}^2$, $\Delta EE$ = 1.40 eV). Moreover, the B3LYP/ROCIS outcomes also indicate that both $\Delta S = 0$ and $\Delta S = -1$ states, both of them associated with single electronic excitations, contribute

to the $^{||/\perp}f(EE)$ distributions. In more detail, $^{||/\perp}L_3{}^1$ features are caused by ΔS = 0 states generated by Cr 2p → SOMOs transitions, with the whole set of the half-occupied Cr 3d-based orbitals ($6e_g$, $21a_{1g}$ and $14b_{2g}$ SOMOs) as *fsos*. At variance with that, the $^{||/\perp}L_3{}^2$ shoulders include contributions from both ΔS = 0 (64%) and ΔS = −1 (30%) states. Quintet states have the same origin as those associated with $^{||/\perp}L_3{}^1$, while the triplet ones are related to Cr-based 2p → $16b_{1g}$ and MLCT 2p → $\pi^*$ Pc-based transitions. As such, it is noteworthy that states associated with the Cr-based 2p → $16b_{1g}$ transition only contribute to $^{||}L_3{}^2$. Analogously to VPc, any comment about the CrPc $L_2$-edge is herein avoided as it cannot be unambiguously determined by experiment [32]; nevertheless, we underline that the B3LYP/ROCIS $L_2$–$L_3{}^1$ $^{HS}\Delta EE$ (8.6 eV, see Figure 4b) fairly reproduces the experimental value (7.9 eV).

*MnPc $L_3$-edge.* The MnPc $L_{2,3}$-edges' XA spectrum recorded by Koshino et al. [33] suffers from the same issues already mentioned for CrPc. Otherwise, the experimental evidence reported by Kroll et al. [34] for MPc ($25 \leq Z \leq 30$) is much more informative as a consequence of the *EE* range they showed for each single MPc, thus allowing the detection of the fine structure eventually contributing to spectral features; moreover, both || and ⊥ polarized XA spectra are reported for each MPc. In the forthcoming discussion, ISEELS outcomes of Koshino et al. will no longer be considered as a reference for the $L_{2,3}$-edges XAS modelling herein presented. At least three well-evident and closely spaced peaks (herein labelled $^{||}L_3{}^1$, $^{||}L_3{}^2$ and $^{||}L_3{}^3$, and lying at ~640.0, ~641.0 and ~643.0 eV, respectively) contribute to the MnPc $^{||}L_3$-edge spectrum (see Figure 4c). In addition, the $^{||}L_3{}^3$'s higher *EE* side is characterized by the presence of an evident shoulder at ~644.0 eV. The || → ⊥ light polarization switching is accompanied by a significant relative intensity reduction in spectral features having *EE*s in between 642 and 644 eV, thus reducing the $^{\perp}L_3$-edge spectrum to the $^{\perp}L_3{}^1$ and $^{\perp}L_3{}^2$ peaks with comparable intensity and lying at ~640.5 and ~641.5 eV, respectively (see Figure 4c).

The MnPc B3LYP/ROCIS $^{||/\perp}f(EE)$ distributions, not herein included, poorly reproduces the $L_3$-edge XA spectrum in terms of number of peaks, relative energy positions and relative intensities. A few years ago, Carlotto et al. [123] tested the efficiencies of several diverse XC functionals (non-hybrid, hybrid and hybrid meta-GGA) in reproducing the $L_{2,3}$-edges' absorption spectra of Mn complexes. The use of the hybrid M06 meta-GGA XC functional [75] was found to be decisive for a detailed assignment of the $Mn(acac)_3$ (acac = acetylacetonato) $L_{2,3}$-edges XAS features. Now, despite the inability even of the M06 XC functional to reproduce in detail the complex structure of the MnPc XA spectrum, in particular the presence of the closely spaced $^{||}L_3{}^1$ and $^{||}L_3{}^2$ peaks, the IS-corresponding modelling (see Figure 4c) provides a satisfactory agreement between experiment and theory. In more detail, theoretical results indicate that the lowest-lying feature of the $^{||}f(EE)$ distribution ($^{||}L_3{}^1$, representative of the $^{||}L_3{}^1$ and $^{||}L_3{}^2$ experimental peaks; see Figure 4c) has to be associated to the quartet electronic states (ΔS = 0) generated by single electronic excitations having the whole Mn 2p set as *isos* and the low-lying Mn 3d-based $21a_{1g}{}^{\downarrow}$, $14b_{2g}{}^{\downarrow}$ and $6e_g{}^{\downarrow}$ VMOs as *fsos*. At variance with that, electronic states with ΔS = 0 (58%) and ΔS = 1 (24%) contribute to the intense $^{||}L_3{}^3$ feature, while electronic states with ΔS = -1 negligibly contribute to the $^{||/\perp}L_3$ patterns. Former states (ΔS = 0) imply Mn 2p → SOMOs ($21a_{1g}$, $14b_{2g}$ and $6e_g$) and SOMOs → $16b_{1g}/7e_g$ coupled-single excitations [25,32], while the latter (ΔS = 1) are mainly generated by Mn 2p → $\pi^*$ Pc-based single electronic excitations. The ΔS = 1 Mn 2p → $\pi^*$ Pc-based $4b_{2u}$ single electronic excitation violates selection rules stated by Eqns 5–8. As such, it has to be mentioned that i) ORCA calculations have to be run in $C_1$ symmetry and ii) the *f* value of the ΔS = 1 Mn 2p → $\pi^*$ Pc-based $4b_{2u}$ single electronic excitation is very low.

The satisfactory agreement between $^{||/\perp}f(EE)$ distributions and experimental evidence [34] prompts us to further detail the proposed assignment. Despite the fact that electronic states generating the $^{||/\perp}L_3{}^1$ features of Figure 4c are associated with Mn-based ΔS = 0 2p → 3d single electronic excitations involving the whole 2p set and the low-lying Mn 3d-based ↓ VMOs, it sounds reasonable that the $(1a_{2u} \rightarrow 21a_{1g})^{\perp}$ and $(1e_u \rightarrow 6e_g)^{\perp}$

transitions contribute to the $L_3$ lower *EE* region more than the $(1a_{2u} \rightarrow 6e_g)^{||}$, $(1e_u \rightarrow 21a_{1g})^{||}$ and $(1e_u \rightarrow 14b_{2g})^{||}$ ones, while the opposite is true when $L_3{}^3$ is considered. In fact, once again in agreement with the experimental results of Kroll et al. [34], the electronic states determined by $\Delta S = 0$, 1 coupled-single and single $\perp$ polarized electronic transitions provide to the $L_3$ higher *EE* region a contribution significantly lower than those $||$ polarized.

DFT/ROCIS calculations fairly reproduce both the $L_2$–$L_3$ $\Delta EE$ (~10 eV) and the corresponding relative intensities; nevertheless, any detailed assignment of the $L_2$ feature is herein avoided as it is not unambiguously determined by experimentation [32,80].

*FePc $L_3$-edge.* FePc has been the object of a huge number of $L_{2,3}$-edges XAS studies [33,34,38,120,124–127]. Among them, Bartolomé et al. [125] investigated the Fe magnetic moment switching in the catalytic ORR of FePc adsorbed on Ag(110) by combining the results of X-ray linear polarized absorption spectroscopy with those of X-ray magnetic circular dichroism at the Fe $L_{2,3}$-edges. A detailed analysis of the $||$ and $\perp$ Fe $L_{2,3}$-edges components of the FePc and FePc($\eta^2$-$O_2$) XA spectra has been recently reported by Carlotto et al. [38] by adopting a computational set-up slightly different from that herein employed. The adopted set of $c_1$, $c_2$, and $c_3$ semi-empirical parameters corresponded to that herein labelled old set; moreover, the saturation of the final-state manifold was obtained by considering forty nonrelativistic roots per multiplicity.

The comparison of the FePc ${}^{||/\perp}f(EE)$ distributions (see Figure S2 of the Supplementary Materials) with the literature's theoretical results [38] proves an evident disagreement. To disentangle the effects induced by the adoption of a particular set of semi-empirical parameters from those generated by the number of nonrelativistic roots per multiplicity, the ${}^{||/\perp}f(EE)$ distributions have been again evaluated by using the $c_1$, $c_2$, and $c_3$ old set (see Figure 4d). Besides minor differences, most likely due to the higher number of states and expansion vectors herein adopted in the iterative solution of the CI equations, the ${}^{||/\perp}f(EE)$ distributions obtained by adopting $c_1 = 0.21$, $c_2 = 0.49$, and $c_3 = 0.29$ substantially mirror the literature's ones [38].

According to Carlotto et al. [38], weighty contributions to the ${}^{||/\perp}f(EE)$ distributions arise from states having a spin multiplicity either equal to ($\Delta S = 0$) or higher/lower ($\Delta S = \pm 1$) than the GS one. More specifically, the ${}^{||/\perp}L_3{}^1$ features lying at the lowest excitation energy (see Figure 4d) are both associated to triplet states ($\Delta S = 0$), and are generated by single electronic excitations with the whole Fe 2p set as *isos* and the low-lying Fe 3d-based $21a_{1g}{}^{\downarrow}$ VMO and $6e_g{}^{\downarrow}$ SOMO as *fsos*. Perfectly in agreement with the well-evidenced experimental dichroism [34,38], ${}^{\perp}L_3{}^1$ is much more intense than ${}^{||}L_3{}^1$, thus indicating that electronic states associated with $(a_{2u} \rightarrow a_{1g})^{\perp}/(e_u \rightarrow e_g)^{\perp}$ excitations contribute much more than the $(a_{2u} \rightarrow e_g)^{||}/(e_u \rightarrow a_{1g})^{||}$ ones to the lower *EE* region of the $L_3$-edge. Excitations with $\Delta S = 0, -1$ comparably participate in states determining ${}^{\perp}L_3{}^2$ (the theoretical set-up herein adopted makes negligible $\Delta S = 1$ contributions). As such, $\Delta S = 0$ electronic excitations involve the Fe-based $6e_g{}^{\downarrow}$ and $21a_{1g}{}^{\downarrow}$ VMO, while the $\Delta S = -1$ ones have an MLCT character and imply Pc-based $\pi^*$ VMOs. Moving to the analysis of the ${}^{||}L_3{}^2$ and ${}^{||}L_3{}^3$ features, the comparison with the XAS evidence indicates that their excitation energies are slightly overestimated with respect to the ${}^{||}L_3{}^1$ one; moreover, electronic states with $\Delta S = 0$ (71%), 1 (19%) and $-1$ (7%) contribute to them. In even more detail, both single (44%) and coupled-single (56%) excitations contribute to the prevailing $\Delta S = 0$ states. The former involves Fe-based $(2p \rightarrow 21a_{1g}{}^{\downarrow}/6e_g{}^{\downarrow}, 2p \rightarrow 16b_{1g})$ and MLCT $(2p \rightarrow 7e_g)$ transitions, while the latter are Fe-based $(2p \rightarrow$ SOMOs and SOMOs $\rightarrow 16b_{1g})$ excitations, determining the states contributing to the ${}^{||}L_3{}^2$ and ${}^{||}L_3{}^3$ lower excitation energy sides.

The DFT/ROCIS calculations [38] fairly reproduce both the $L_2$–$L_3$ $\Delta EE$ (~13 eV) and the corresponding relative intensities; nevertheless, any detailed assignment of the $L_2$ feature is herein avoided as it is not unambiguously determined by experimentation [32,80].

## 4. Conclusions

The occupied and empty states of HS VPc, CrPc, IS MnPc and FePc have been thoroughly investigated by exploiting the original/homogeneous theoretical results and experimental evidence form the literature. The use of the Hirshfeld charges [84] coupled with the Nalewajski−Mrozek [66–71] approach ultimately indicates that, among the investigated molecules, FePc is characterized by the strongest and most covalent M–Pc $\sigma$ interaction. Even though Slater's transition state calculations ultimately confirm the Berkowitz hypothesis that, for FePc, " ... the first ionization potential corresponds to electron ejection from a ring orbital, and not a metal orbital", the extension of the method to lighter MPcs reveals significant differences, the rationale of which lies with the relative energy position of the $Pc^{2-}$-based and $M^{II}$ 3d-based occupied/half-occupied MOs. Insights into the MPcs' virtual electronic structure have been gained by revisiting XAS data from the literature in light of DFT/ROCIS calculations. The higher *EE* side of the MPc $L_3$-edge XA spectra systematically includes states associated with MLCT transitions, most of them involving the metal 2p $\rightarrow$ $Pc^{2-}$-based $7e_g$ $\pi^*$ VMO excitations; moreover, the same *EE* region of all but one of (VPc) the $L_3$-edge XA spectra is characterized by the presence of electronic states associated with M-based 2p $\rightarrow$ $16b_{1g}$ excitations. The agreement between theory and experiment is satisfactory, but it required a "tuning" of the modelling set-up in terms of XC functionals and/or $c_1$, $c_2$, and $c_3$ semiempirical parameters. As a final consideration, we underline that the theoretical outcomes obtained for the HS MPc (VPc and CrPc) are a true challenge for the experimental community called upon to confirm or deny them.

**Supplementary Materials:** The following are available online at https://www.mdpi.com/2079-4991/11/1/54/s1, Figure S1: 3D plot of the MnPc $6e_g^{\downarrow}$ MO. Displayed isosurfaces correspond to $\pm 0.015\ e^{1/2} \times A^{-3/2}$; Figure S2: $^{IS}$FePc $^{||/\perp}f(EE)$ distributions estimated by adopting $c_1 = 0.18$, $c_2 = 0.20$, and $c_3 = 0.40$. Blue and red lines correspond to $||$ and $\perp$ components, respectively. Simulated spectra have a Gaussian broadening of 1.5 eV. Table S1: Optimized BP86 Cartesian coordinates for HS VPc; Table S2: Optimized BP86 Cartesian coordinates for HS CrPc; Table S3: Optimized BP86 Cartesian coordinates for IS MnPc; Table S4: Optimized BP86 Cartesian coordinates for IS FePc; Table S5: Symmetries of a $2p^53d^{4/6}$ system; Table S6: Symmetries of a $2p^53d^5$ system; Table S7: Symmetries of a $2p^53d^7$ system.

**Author Contributions:** Methodology, analysis, investigation, and writing—original draft preparation: S.C., M.S., F.S. and A.V.; review and editing, supervision: M.C.; funding acquisition: S.C. and M.C. All authors have read and agreed to the published version of the manuscript.

**Funding:** This research was supported by the University of Padova (Grant P-DISC #CARL-SID17 BIRD2017-UNIPD, Project CHIRoN).

**Institutional Review Board Statement:** Not Applicable.

**Informed Consent Statement:** Not Applicable.

**Data Availability Statement:** All data have been illustrated in the manuscript and in the supplementary materials.

**Acknowledgments:** The Computational Chemistry Community ($C_3P$) of the University of Padova is kindly acknowledged.

**Conflicts of Interest:** All authors of this manuscript directly participated in the planning, execution, and analysis of this study. The contents of this manuscript have not been copyrighted or published previously and are not currently under consideration for publication elsewhere. The contents of this manuscript will not be copyrighted, submitted, or published elsewhere after acceptance by NANOMATERIALS.

## References

1. Ghosh, A. *Letters to a Young Chemist*; John Wiley & Sons: Hoboken, NJ, USA, 2011; p. 34.
2. *Functional Phthalocyanine Molecular Materials*; Springer: Berlin/Heidelberg, Germany, 2010; Volume 135.
3. Wöhrle, D.; Schnurpfeil, G.; Makarov, S.G.; Kazarin, A.; Suvorova, O.N. Practical Applications of Phthalocyanines—From Dyes and Pigments to Materials for Optical, Electronic and Photo-electronic Devices. *Macroheterocycles* **2012**, *5*, 191–202. [CrossRef]

4. Angione, M.D.; Pilolli, R.; Cotrone, S.; Magliulo, M.; Mallardi, A.; Palazzo, G.; Sabbatini, L.; Fine, D.; Dodabalapur, A.; Cioffi, N.; et al. Carbon based materials for electronic bio-sensing. *Mater. Today* **2011**, *14*, 424–433. [CrossRef]
5. Jang, S.H.; Jen, A.K.Y. Structured Organic Non-Linear Optics. *Compr. Nanosci. Technol.* **2011**, *1*, 143–187.
6. Nguyen, T. Polymer-based nanocomposites for organic optoelectronic devices. *Surf. Coat. Technol.* **2011**, *206*, 742–752. [CrossRef]
7. Hains, A.W.; Liang, Z.; Woodhouse, M.A.; Gregg, B.A. Molecular Semiconductors in Organic Photovoltaic Cells. *Chem. Rev.* **2010**, *110*, 6689–6735. [CrossRef] [PubMed]
8. Cao, W.; Xue, J. Recent progress in organic photovoltaics: Device architecture and optical design. *Energy Environ. Sci.* **2014**, *7*, 2123–2144. [CrossRef]
9. Sorokin, A.B. Phthalocyanine Metal Complexes in Catalysis. *Chem. Rev.* **2013**, *113*, 8152–8191. [CrossRef]
10. Tolman, W.B.; Solomon, E.I. Preface: Forum on Dioxygen Activation and Reduction. *Inorg. Chem.* **2010**, *49*, 3555–3556. [CrossRef]
11. Scherson, D.A.; Palencsár, A.; Tolmachev, Y.; Stefan, I. Transition Metal Macrocycles as Electrocatalysts for Dioxygen Reduction. In *Electrochemical Surface Modification: Thin Films, Functionalization and Characterization*; Alkire, R.C., Kolb, D.M., Lipkowski, J., Ross, P.N., Eds.; Wiley-VCH: Weinheim, Germany, 2008; pp. 191–288.
12. Sedona, F.; Di Marino, M.; Forrer, D.; Vittadini, A.; Casarin, M.; Cossaro, A.; Floreano, L.; Verdini, A.; Sambi, M. Tuning the Catalytic Activity of Ag(110)-supported Fe Phthalocyanine in the Oxygen Reduction Reaction. *Nat. Mater.* **2012**, *11*, 970–977. [CrossRef]
13. Bianconi, A. XANES Spectroscopy. In *X-ray Absorption: Principles, Applications, Techniques of EXAFS, SEXAFS and XANES*; Koningsberger, D.C., Prins, R., Eds.; John Wiley & Sons: New York, NY, USA, 1988; pp. 573–662.
14. Stöhr, J. *NEXAFS Spectroscopy*; Springer: Berlin, Germany, 1996.
15. Zhang, H.H.; Hedman, B.; Hodgson, K.O. X-ray Absorption Spectroscopy and EXAFS Analysis. The Multiple-Scattering Method and Applications in Inorganic and Bioinorganic Chemistry. In *Inorganic Electronic Structure and Spectroscopy*; Solomon, E.I., Lever, A.B.P., Eds.; John Wiley & Sons: New York, NY, USA, 1999; Volume 1, pp. 513–554.
16. Solomon, E.I.; Bell, C.B., III. Inorganic and Bioinorganic Spectroscopy. In *Physical Inorganic Chemistry, Principle, Methods and Models*; Bakac, A., Ed.; John Wiley & Sons: New York, NY, USA, 2010; pp. 1–37.
17. Douglas, B.E.; Hollingsworth, C.A. *Symmetry in Bonding and Spectra, an Introduction*; Academic Press: Orlando, FL, USA, 1985.
18. Neese, F.; Hedman, B.; Hodgson, K.O.; Solomon, E.I. Relationship between the Dipole Strength of Ligand Pre-Edge Transitions and Metal−Ligand Covalency. *Inorg. Chem.* **1999**, *38*, 4854–4860. [CrossRef]
19. Glaser, T.; Hedman, B.; Hodgson, L.O.; Solomon, E.I. Ligand K-Edge X-ray Absorption Spectroscopy: A Direct Probe of Ligand−Metal Covalency. *Acc. Chem. Res.* **2000**, *33*, 859–868. [CrossRef] [PubMed]
20. Solomon, E.I.; Hedman, B.; Hodgson, K.O.; Dey, A.; Szilagyi, R.K. Ligand K-edge x-ray absorption spectroscopy: Covalency of ligand-metal bonds. *Coord. Chem. Rev.* **2005**, *249*, 97–129. [CrossRef]
21. Baker, M.-L.; Mara, M.W.; Yan, J.J.; Hodgson, K.O.; Hedman, B.; Solomon, E.I. K- And L-edge X-ray Absorption Spectroscopy (XAS) and Resonant Inelastic X-ray Scattering (RIXS) Determination of Differential Orbital Covalency (DOC) of Transition Metal Sites. *Coord. Chem. Rev.* **2017**, *345*, 182–208. [CrossRef] [PubMed]
22. Jørgensen, C.K. *Absorption Spectra and Chemical Bonding in Complexes*; Pergamon Press: Oxford, UK, 1962; p. 77.
23. de Groot, F. Multiplet effects in X-ray spectroscopy. *Coord. Chem. Rev.* **2005**, *249*, 31–63. [CrossRef]
24. de Groot, F.; Kotani, A. *Core Level Spectroscopy of Solids*; CRC Press: Boca Raton, FL, USA, 2008.
25. Roemelt, M.; Neese, F. Excited States of Large Open-Shell Molecules: An Efficient, General, and Spin-Adapted Approach Based on a Restricted Open-Shell Ground State Wave function. *J. Phys. Chem. A* **2013**, *117*, 3069–3083. [CrossRef]
26. Bagus, P.S.; Freund, H.; Kuhlenbeck, H.; Ilton, E.S. A new analysis of X-ray adsorption branching ratios: Use of Russell−Saunders coupling. *Chem. Phys. Lett.* **2008**, *455*, 331–334. [CrossRef]
27. Ikeno, H.; Mizoguchi, T.; Tanaka, I. Ab initio charge transfer multiplet calculations on the $L_{2,3}$ XANES and ELNES of 3d transition metal oxides. *Phys. Rev. B: Condens. Matter Mater. Phys.* **2011**, *83*, 155107. [CrossRef]
28. Josefsson, I.; Kunnus, K.; Schreck, S.; Föhlisch, A.; de Groot, F.; Wernet, P.; Odelius, M. Ab Initio calculations of x-ray spectra: Atomic multiplet and molecular orbital effects in a multiconfigurational SCF approach to the L-edge spectra of transition metal complexes. *J. Phys. Chem. Lett.* **2012**, *3*, 3565–3570. [CrossRef]
29. Maganas, D.; Roemelt, M.; Hävecker, M.; Trunschke, A.; Knop-Gericke, A.; Schlögl, R.; Neese, F. First principles calculations of the structure and V L-edge X-ray absorption spectra of $V_2O_5$ using local pair natural orbital coupled cluster theory and spin−orbit coupled configuration interaction approaches. *Phys. Chem. Chem. Phys.* **2013**, *15*, 7260–7276. [CrossRef]
30. Roemelt, M.; Maganas, D.; DeBeer, S.; Neese, F. A combined DFT and restricted open-shell configuration interaction method including spin-orbit coupling: Application to transition metal L-edge X-ray absorption spectroscopy. *J. Chem. Phys.* **2013**, *138*, 204101 (1:22). [CrossRef]
31. Maganas, D.; DeBeer, S.; Neese, F. Restricted open-shell configuration interaction cluster calculations of the L-edge x-ray absorption study of $TiO_2$ and $CaF_2$ solids. *Inorg. Chem.* **2014**, *53*, 6374–6385. [CrossRef] [PubMed]
32. Maganas, D.; Roemelt, M.; Weyhermüller, T.; Blume, R.; Hävecker, M.; Knop-Gericke, A.; DeBeer, S.; Schlögl, R.; Neese, F. L-edge X-ray absorption study of mononuclear vanadium complexes and spectral predictions using a restricted open shell configuration interaction ansatz. *Phys. Chem. Chem. Phys.* **2014**, *16*, 264–276. [CrossRef] [PubMed]
33. Koshino, M.; Kurata, H.; Isoda, S.; Kobayashi, T. Branching ratio and $L_2$ + $L_3$ intensities of 3d-transition metals in phthalocyanines and the amine complexes. *Micron* **2000**, *31*, 373–380. [CrossRef]

34. Kroll, T.; Kraus, R.; Schönfelder, R.; Aristov, V.Y.; Molodtsova, O.V.; Hoffmann, P.; Knupfer, M. Transition metal phthalocyanines: Insight into the electronic structure from soft x-ray spectroscopy. *J. Chem. Phys.* **2012**, *137*, 054306. [CrossRef]
35. Eguchi, K.; Nakagawa, T.; Takagi, Y.; Yokoyama, T. Direct Synthesis of Vanadium Phthalocyanine and Its Electronic and Magnetic States in Monolayers and Multilayers on Ag(111). *J. Phys. Chem. C* **2015**, *119*, 9805–9815. [CrossRef]
36. Carlotto, S.; Sambi, M.; Rancan, M.; Casarin, M. Theoretical Investigation of the Electronic Properties of Three Vanadium Phthalocyaninato (Pc) Based Complexes: PcV, PcVO, and PcVI. *Inorg. Chem.* **2018**, *57*, 1859–1869. [CrossRef]
37. Casarin, M.; Carlotto, S. Pigments of Life", Molecules Well Suited to Investigate Metal–Ligand Symmetry-Restricted Covalency. *Eur. J. Inorg. Chem.* **2018**, 3145–3155. [CrossRef]
38. Carlotto, S.; Sambi, M.; Sedona, F.; Vittadini, A.; Bartolomé, J.; Bartolomé, F.; Casarin, M. $L_{2,3}$-edges absorption spectra of a 2D complex system: A theoretical modelling. *Phys. Chem. Chem. Phys.* **2016**, *18*, 28110–28116. [CrossRef]
39. Nardi, M.V.; Detto, F.; Aversa, L.; Verucchi, R.; Salviati, G.; Iannotta, S.; Casarin, M. Electronic properties of CuPc and $H_2$Pc: An experimental and theoretical study. *Phys. Chem. Chem. Phys.* **2013**, *15*, 12864–12881. [CrossRef]
40. Mangione, G.; Sambi, M.; Nardi, M.V.; Casarin, M. A theoretical study of the $L_3$ pre-edge XAS in Cu(II) complexes. *Phys. Chem. Chem. Phys.* **2014**, *16*, 19852–19855. [CrossRef]
41. Mangione, G.; Sambi, M.; Carlotto, S.; Vittadini, A.; Ligorio, G.; Timpel, M.; Pasquali, L.; Giglia, A.; Nardi, M.V.; Casarin, M. Electronic structure of CuTPP and CuTPP(F) complexes: A combined experimental and theoretical study II. *Phys. Chem. Chem. Phys.* **2016**, *18*, 24890–24904. [CrossRef] [PubMed]
42. Neese, F.; Wiley. The ORCA program system. *Interdiscip. Rev. Comput. Mol. Sci.* **2012**, *2*, 73–78. [CrossRef]
43. Wang, F.; Ziegler, T. The calculation of excitation energies based on the relativistic two-component zeroth-order regular approximation and time-dependent density-functional with full use of symmetry. *J. Chem. Phys.* **2005**, *122*, 204103. [CrossRef] [PubMed]
44. Hirata, S.; Head-Gordon, M. Time-dependent density functional theory within the Tamm–Dancoff approximation. *Chem. Phys. Lett.* **1999**, *314*, 291–299. [CrossRef]
45. Carlotto, S.; Floreano, L.; Cossaro, A.; Dominguez, M.; Rancan, M.; Sambi, M.; Casarin, M. The electronic properties of three popular high spin complexes [$TM(acac)_3$, TM = Cr, Mn, and Fe] revisited: An experimental and theoretical study. *Phys. Chem. Chem. Phys.* **2017**, *19*, 24840–24854. [CrossRef]
46. Casarin, M.; Finetti, P.; Vittadini, A.; Wang, F.; Ziegler, T. Spin-Orbit Relativistic Time-Dependent Density Functional Calculations of the Metal and Ligand Pre-Edge XAS Intensities of Organotitanium Complexes: $TiCl_4$, Ti($\eta^5$-$C_5H_5$)$Cl_3$, and Ti($\eta^5$-$C_5H_5$)$_2Cl_2$. *J. Phys. Chem. A* **2007**, *111*, 5270–5279. [CrossRef]
47. Carlotto, S.; Finetti, P.; de Simone, M.; Coreno, M.; Casella, G.; Sambi, M.; Casarin, M. Comparative Experimental and Theoretical Study of the C and O K-Edge X-ray Absorption Spectroscopy in Three Highly Popular, Low Spin Organoiron Complexes: $[Fe(CO)_5]$, [($\eta^5$-$C_5H_5$)Fe(CO)($\mu$-CO)]$_2$, and [($\eta^5$-$C_5H_5$)$_2$Fe]. *Inorg. Chem.* **2019**, *58*, 16411–16423. [CrossRef]
48. Carlotto, S.; Finetti, P.; de Simone, M.; Coreno, M.; Casella, G.; Sambi, M.; Casarin, M. Comparative Experimental and Theoretical Study of the Fe $L_{2,3}$-Edges X-ray Absorption Spectroscopy in Three Highly Popular, Low Spin Organoiron Complexes: $[Fe(CO)_5]$, [($\eta^5$-$C_5H_5$)Fe(CO)($\mu$-CO)]$_2$, and [($\eta^5$-$C_5H_5$)$_2$Fe]. *Inorg. Chem.* **2019**, *58*, 5844–5857. [CrossRef]
49. Wu, W.; Harrison, N.M.; Fisher, A.J. Suitability of chromium phthalocyanines to test Haldane's conjecture: First-principles calculations. *Phys. Rev. B: Condens. Matter Mater. Phys.* **2013**, *88*, 224417. [CrossRef]
50. Li, Y.; Sun, Q. The superior catalytic CO oxidation capacity of a Cr-phthalocyanine porous sheet. *Sci. Rep.* **2014**, *4*, 4098. [CrossRef]
51. Junkaew, A.; Meeprasert, J.; Jansang, B.; Kungwan, N.; Namuangruk, S. Mechanistic study of NO oxidation on Cr–phthalocyanine: Theoretical insight. *RSC Adv.* **2017**, *7*, 8858–8865. [CrossRef]
52. Liu, K.; Lei, Y.; Wang, G. Correlation between oxygen adsorption energy and electronic structure of transition metal macrocyclic complexes. *J. Chem. Phys.* **2013**, *139*, 204306. [CrossRef] [PubMed]
53. Bala, M.; Verma, P.K.; Sharma, U.; Kumar, N.; Singh, B. Iron phthalocyanine as an efficient and versatile catalyst for *N*-alkylation of heterocyclic amines with alcohols: One-pot synthesis of 2-substituted benzimidazoles, benzothiazoles and benzoxazoles. *Green Chem.* **2013**, *15*, 1687–1693. [CrossRef]
54. Paradine, S.M.; White, M.C. Iron-Catalyzed Intramolecular Allylic C–H Amination. *J. Am. Chem. Soc.* **2012**, *134*, 2036–2039. [CrossRef] [PubMed]
55. Lamar, A.A.; Nicholas, K.M. Direct synthesis of 3-arylindoles via annulation of aryl hydroxylamines with alkynes. *Tetrahedron* **2009**, *65*, 3829–3833. [CrossRef]
56. Taniguchi, T.; Hirose, D.; Ishibashi, H. Esterification via Iron-Catalyzed Activation of Triphenylphosphine with Air. *ACS Catal.* **2011**, *1*, 1469–1474. [CrossRef]
57. Prateeptongkum, S.; Jovel, I.; Jackstell, R.; Vogl, N.; Weckbecker, C.; Beller, M. First iron-catalyzed synthesis of oximes from styrenes. *Chem. Commun.* **2009**, 1990–1992. [CrossRef]
58. Kudrik, E.; Makarov, S.V.; Zahl, A.; van Eldik, R. Mechanism of the Iron Phthalocyanine Catalyzed Reduction of Nitrite by Dithionite and Sulfoxylate in Aqueous Solution. *Inorg. Chem.* **2005**, *44*, 6470–6475. [CrossRef]
59. Sugimori, T.; Horike, S.I.; Tsumura, S.; Hande, M.; Kasuga, K. Catalytic oxygenation of olefin with dioxygen and tetra-t-butylphthalocyanine complexes in the presence of sodium borohydride. *Inorg. Chim. Acta* **1998**, *283*, 275–278. [CrossRef]
60. Leggans, E.K.; Barker, T.J.; Duncan, K.K.; Boger, D.L. Iron(III)/NaBH4-Mediated Additions to Unactivated Alkenes: Synthesis of Novel 20′-Vinblastine Analogues. *Org. Lett.* **2012**, *14*, 1428–1431. [CrossRef]

61. Taniguchi, T.; Goto, N.; Nishibata, A.; Ishibashi, H. Iron-Catalyzed Redox Radical Cyclizations of 1,6-Dienes and Enynes. *Org. Lett.* **2010**, *12*, 112–115. [CrossRef] [PubMed]
62. Auwärter, W.; Écija, D.; Klappenberger, E.; Barth, J.V. Porphyrins at interfaces. *Nat. Chem.* **2015**, *7*, 105–120. [CrossRef] [PubMed]
63. ADF2014, SCM, Theoretical Chemistry, Vrije Universiteit, Amsterdam, The Netherlands. Available online: http://www.scm.com (accessed on 28 December 2020).
64. Becke, A.D. Density-functional exchange-energy approximation with correct asymptotic behaviour. *Phys. Rev. A: At. Mol. Opt. Phys.* **1988**, *38*, 3098–3100. [CrossRef] [PubMed]
65. Perdew, J.P. Density functional approximation for the correlation energy of the inhomogeneous electron gas. *Phys. Rev. B Condens. Matter Mater. Phys.* **1986**, *33*, 8822–8824. [CrossRef]
66. Nalewajski, R.F.; Mrozek, J. Modified valence indices from the two-particle density matrix. *Int. J. Quantum Chem.* **1994**, *51*, 187–200. [CrossRef]
67. Nalewajski, R.F.; Mrozek, J.; Formosinho, S.J.; Varandas, A.J.C. Quantum mechanical valence study of a bond-breaking−bond forming process in triatomic systems. *Int. J. Quantum Chem.* **1994**, *52*, 1153–1176. [CrossRef]
68. Nalewajski, R.F.; Mrozek, J. Hartree-Fock difference approach to chemical valence: Three-electron indices in UHF approximation. *Int. J. Quantum Chem.* **1996**, *57*, 377–389. [CrossRef]
69. Nalewajski, R.F.; Mrozek, J.; Mazur, G. Quantum chemical valence indices from the one-determinantal difference approach. *Can. J. Chem.* **1996**, *74*, 1121–1130. [CrossRef]
70. Nalewajski, R.F.; Mrozek, J.; Michalak, A. Two-electron valence indices from the Kohn-Sham orbitals. *Int. J. Quantum Chem.* **1997**, *61*, 589–601. [CrossRef]
71. Nalewajski, R.F.; Mrozek, J.; Michalak, A. Exploring bonding patterns of molecular systems using quantum mechanical bond multiplicities. *Polym. J. Chem.* **1998**, *72*, 1779–1791.
72. Michalak, A.; DeKock, R.L.; Ziegler, T. Bond Multiplicity in Transition-Metal Complexes: Applications of Two-Electron Valence Indices. *J. Phys. Chem. A* **2008**, *112*, 7256–7263. [CrossRef]
73. Ziegler, T.; Rauk, A. On the calculation of bonding energies by the Hartree Fock Slater method. *Theor. Chim. Acta* **1977**, *46*, 1–10. [CrossRef]
74. Becke, A.D. Density-functional thermochemistry. III. The role of exact exchange. *J. Chem. Phys.* **1993**, *98*, 5648–5652. [CrossRef]
75. Zhao, Y.; Truhlar, D.J. The M06 suite of density functionals for main group thermochemistry, thermochemical kinetics, noncovalent interactions, excited states, and transition elements: Two new functionals and systematic testing of four M06-class functionals and 12 other functionals. *Theor. Chem. Acc.* **2008**, *120*, 215–241.
76. Weigend, F.; Ahlrichs, R. Balanced basis sets of split valence, triple zeta valence and quadruple zeta valence quality for H to Rn: Design and assessment of accuracy. *Phys. Chem. Chem. Phys.* **2005**, *7*, 3297–3305. [CrossRef] [PubMed]
77. Weigend, F. Accurate Coulomb-fitting basis sets for H to Rn. *Phys. Chem. Chem. Phys.* **2006**, *8*, 1057–1065. [CrossRef]
78. Pantazis, D.A.; Chen, X.Y.; Landis, C.R.; Neese, F. All-electron scalar relativistic basis sets for third-row transition metal atoms. *J. Chem. Theory Comput.* **2008**, *4*, 908–919. [CrossRef]
79. Lebedev, V.I. Values of the nodes and weights of quadrature formulas of Gauss−Markov type for a sphere from the ninth to seventeenth order of accuracy that are invariant with respect to an octahedron group with inversion. *Zhurnal Vychislitel'noi Mat. Mat. Fiz.* **1975**, *15*, 48–54.
80. Coster, D.; Kronig, R.D.L. A new type of Auger effect and its influence on the X-ray spectrum. *Physica* **1935**, *2*, 13–24. [CrossRef]
81. Mangione, G.; Carlotto, S.; Sambi, M.; Ligorio, G.; Timpel, M.; Vittadini, A.; Nardi, M.V.; Casarin, M. Electronic structures of CuTPP and CuTPP(F) complexes. A combined experimental and theoretical study I. *Phys. Chem. Chem. Phys.* **2016**, *18*, 18727–18738. [CrossRef]
82. Arillo-Flores, O.I.; Fadlallah, M.M.; Schuster, C.; Eckern, U.; Romero, A.H. Magnetic, electronic and vibrational properties of metal and fluorinated metal phthalocyanines. *Phys. Rev. B: Condens. Matter Mater. Phys.* **2013**, *87*, 165115. [CrossRef]
83. Jahn, H.; Teller, E. Stability of polyatomic molecules in degenerate electronic states-I—Orbital degeneracy. *Proc. R. Soc. London, Ser. A* **1937**, *161*, 220–235.
84. Hirshfeld, F.L. Bonded-atom fragments for describing molecular charge densities. *Theor. Chim. Acta* **1977**, *44*, 129–138. [CrossRef]
85. Slater, J.C. *Quantum Theory of Molecules and Solids. The Self-Consistent-Field for Molecules and Solids*; McGraw-Hill: New York, NY, USA, 1974.
86. Liberman, D.A. Slater transition-state band-structure calculations. *Phys. Rev. B: Condens. Matter Mater. Phys.* **2000**, *62*, 6851–6853. [CrossRef]
87. Berkowitz, J. Photoelectron spectroscopy of phthalocyanine vapors. *J. Chem. Phys.* **1979**, *70*, 2819–2828. [CrossRef]
88. A comprehensive collection of single-crystal structures of phthalocyanine complexes and related macrocycles is reported in M.K. Engel. In *The Porphyrin Handbook*; Phthalocyanines: Structural Characterization; Academic Press: New York, NY, USA, 2003; Volume 20, pp. 1–242.
89. Elvidge, J.A.; Lever, B.P. Metal chelates. Part II. Phthalocyanine–chromium complexes and perpendicular conjugation. *J. Chem. Soc.* **1961**, 1257–1265. [CrossRef]
90. Lever, A.B.P. The magnetic behaviour of transition-metal phathalocyanines. *J. Chem. Soc.* **1965**, 1821–1829. [CrossRef]
91. Soler, J.M.; Artacho, E.; Gale, J.D.; García, A.; Junquera, J.; Ordejón, P.; Sánchez-Portal, D. The SIESTA method for ab initio order-N materials simulation. *J. Phys. Condens. Matter* **2002**, *14*, 2745–2779. [CrossRef]

92. Figgis, B.N.; Mason, R.; Williams, G.A. Structure of Phthalocyaninatomanganese(II) at 5.8 K Determined by Neutron Diffraction. *Acta Cryst.* **1980**, *B36*, 2963–2970. [CrossRef]
93. Kirner, J.F.; Dow, D.; Scheidt, W.R. Molecular Stereochemistry of Two Intermediate-Spin Complexes. Iron(II) Phthalocyanine and Manganese(II) Phthalocyanine. *Inorg. Chem.* **1976**, *15*, 1685–1690. [CrossRef]
94. Barraclough, C.G.; Martin, R.L.; Mitra, S.; Sherwood, R.C. Paramagnetic Anisotropy, Electronic Structure, and Ferromagnetism in Spin S = 3/2 Manganese(II) Phthalocyanine. *J. Chem. Phys.* **1970**, *53*, 1638–1642. [CrossRef]
95. Mitra, S.; Greson, A.K.; Hatfield, W.E.; Weller, R.R. Single-Crystal Magnetic Study on Ferromagnetic Manganese(II) Phthalocyaninate. *Inorg. Chem.* **1983**, *22*, 1729–1732. [CrossRef]
96. Williamson, B.E.; van Cott, T.C.; Boyle, M.E.; Misener, C.G.; Stillman, M.J.; Schatz, P.N. Determination of the Ground State of Manganese Phthalocyanine in an Argon Matrix Using Magnetic Circular Dichroism and Absorption Spectroscopy. *J. Am. Chem. Soc.* **1992**, *114*, 2412. [CrossRef]
97. Taguchi, Y.; Miyake, T.; Margadonna, S.; Kato, K.; Prassides, K.; Iwasa, Y. Synthesis, Structure, and Magnetic Properties of Li-Doped Manganese-Phthalocyanine, $Li_x$[MnPc] ($0 \leq x \leq 4$). *J. Am. Chem. Soc.* **2006**, *128*, 3313. [CrossRef]
98. Petraki, F.; Peisert, H.; Hoffmann, P.; Uihlein, J.; Knupfer, M.; Chassé, T. Modification of the 3d-Electronic Configuration of Manganese Phthalocyanine at the Interface to Gold. *J. Phys. Chem. C* **2012**, *116*, 5121–5127. [CrossRef]
99. Kataoka, T.; Sakamoto, Y.; Yamazaki, Y.; Singh, V.R.; Fujimori, A.; Takeda, Y.; Ohkochic, T.; Fujimori, S.I.; Okane, T.; Saitoh, Y.; et al. Electronic configuration of Mn ions in the $\pi$-d molecular ferromagnet β-Mn phthalocyanine studied by soft X-ray magnetic circular dichroism. *Solid State Commun.* **2012**, *152*, 806–809. [CrossRef]
100. Gottfriedl, J.M. Surface chemistry of porphyrins and phthalocyanines. *Surf. Sci. Reports* **2015**, *70*, 259–379. [CrossRef]
101. Liao, M.S.; Scheiner, S. Electronic structure and bonding in metal phthalocyanines, Metal = Fe, Co, Ni, Cu, Zn, Mg. *J. Chem. Phys.* **2001**, *114*, 9780–9791. [CrossRef]
102. Liao, M.S.; Watts, J.D.; Huang, M.J. DFT Study of Unligated and Ligated ManganeseII Porphyrins and Phthalocyanines. *Inorg. Chem.* **2005**, *44*, 1941–1949. [CrossRef]
103. Marom, N.; Kronik, L. Density functional theory of transition metal phthalocyanines, II: Electronic structure of MnPc and FePc—symmetry and symmetry breaking. *Appl. Phys. A* **2009**, *95*, 165–172. [CrossRef]
104. Shen, X.; Sun, L.; Benassi, E.; Shen, Z.; Zhao, X.; Sanvito, S.; Hou, S. Spin filter effect of manganese phthalocyanine contacted with single-walled carbon nanotube electrodes. *J. Chem. Phys.* **2010**, *132*, 054703. [CrossRef]
105. Brumboiu, I.E.; Totani, R.; de Simone, M.; Coreno, M.; Grazioli, C.; Lozzi, L.; Herper, H.C.; Sanyal, B.; Eriksson, O.; Pugli, C.; et al. Elucidating the 3d Electronic Configuration in Manganese Phthalocyanine. *J. Phys. Chem. A* **2014**, *118*, 927–932. [CrossRef]
106. Wäckerlin, C.; Donati, F.; Singha, A.; Baltic, R.; Uldry, A.C.; Delley, B.; Rusponi, S.; Dreiser, J. Strong antiferromagnetic exchange between manganese phthalocyanine and ferromagnetic europium oxide. *Chem. Comm.* **2015**, *51*, 12958–12961. [CrossRef]
107. Wang, J.; Shi, Y.; Cao, J.; Wu, R. Magnetization and magnetic anisotropy of metallophthalocyanine molecules from the first principles calculations. *Appl. Phys. Lett.* **2009**, *94*, 122502. [CrossRef]
108. Grobosch, M.; Mahns, B.; Loose, C.; Friedrich, R.; Schmidt, C.; Kortus, J.; Knupfer, M. Identification of the electronic states of manganese phthalocyanine close to the Fermi level. *Chem. Phys. Lett.* **2011**, *505*, 122–125. [CrossRef]
109. Grobosch, M.; Aristov, V.Y.; Molodtsova, O.V.; Schmidt, C.; Doyle, B.P.; Nannarone, S.; Knupfer, M. Engineering of the Energy Level Alignment at Organic Semiconductor Interfaces by Intramolecular Degrees of Freedom: Transition Metal Phthalocyanines. *J. Phys. Chem. C* **2009**, *113*, 13219–13222. [CrossRef]
110. Dale, B.W.; Williams, R.J.P.; Johnson, C.E.; Thorp, T.L. S=1 Spin State of Divalent Iron. I. Magnetic Properties of Phthalocyanine Iron (II). *J. Chem. Phys.* **1968**, *49*, 3441–3444. [CrossRef]
111. Dale, B.W.; Williams, R.J.P.; Johnson, C.E.; Thorp, T.L. S=1 Spin State of Divalent Iron. II. A Mössbauer-Effect Study of Phthalocyanine Iron (II). *J. Chem. Phys.* **1968**, *49*, 3445–3449. [CrossRef]
112. Coppens, P.; Li, L.; Zhu, N.J. Electronic ground state of iron(II) phthalocyanine as determined from accurate diffraction data. *J. Am. Chem. Soc.* **1983**, *105*, 6173–6174. [CrossRef]
113. Evangelisti, M.; Bartolomé, J.; de Jongh, L.J.; Filoti, G. Magnetic properties of α-iron(II) phthalocyanine. *Phys. Rev. B Condens. Matter Mater. Phys.* **2002**, *66*, 144410. [CrossRef]
114. Filoti, G.; Kuz'min, M.D.; Bartolomé, J. Mössbauer study of the hyperfine interactions and spin dynamics in α-iron(II) phthalocyanin. *Phys. Rev. B Condens. Matter Mater. Phys.* **2006**, *74*, 134420. [CrossRef]
115. Liao, M.S.; Scheiner, S. Comparative study of metal-porphyrins, -porphyrazines, and -phthalocyanines. *J. Comput. Chem.* **2002**, *23*, 1391–1403. [CrossRef]
116. Mangione, G.; Pandolfo, L.; Sambi, M.; Ligorio, G.; Nardi, M.V.; Cossaro, A.; Floreano, L.; Casarin, M. Ligand-Field Strength and Symmetry-Restricted Covalency in Cu II Complexes—A Near-Edge X-ray Absorption Fine Structure Spectroscopy and Time-Dependent DFT Study. *Eur. J. Inorg. Chem.* **2015**, 2709–2713.
117. Nardi, M.V.; Verucchi, R.; Pasquali, L.; Giglia, A.; Fronzoni, G.; Sambi, M.; Mangione, G.; Casarin, M. XAS of tetrakis(phenyl)- and tetrakis (pentafluorophenyl)-porphyrin: An experimental and theoretical study. *Phys. Chem. Chem. Phys.* **2015**, *17*, 2001–2011. [CrossRef]
118. Carlotto, S.; Sambi, M.; Vittadini, A.; Casarin, M. Theoretical modelling of the $L_{2,3}$-edge X-ray absorption spectra of $Mn(acac)_2$ and $Co(acac)_2$ complexes. *Phys. Chem. Chem. Phys.* **2016**, *18*, 2242–2249. [CrossRef]

119. Carlotto, S.; Casella, G.; Floreano, L.; Verdini, A.; Ribeiro, A.P.C.; Martins, L.M.D.R.S.; Casarin, M. Spin state, electronic structure and bonding on C-scorpionate [Fe(II)$Cl_2$(tpm)] catalyst: An experimental and computational study. *Catal. Tod.* **2020**, *358*, 403–411. [CrossRef]
120. Cojocariu, I.; Carlotto, S.; Sturmeit, H.M.; Zamborlini, G.; Cinchetti, M.; Cossaro, A.; Verdini, A.; Floreano, L.; Jugovac, M.; Puschnig, P.; et al. Ferrous to ferric transition in Fe-phthalocyanine driven by $NO_2$ exposure. *Chem.-Eur. J.*. in press. [CrossRef]
121. Ballhausen, C.J. *Introduction to Ligand Field Theory*; McGraw-Hill Book Company, Inc.: New York, NY, USA, 1962; p. 69.
122. Sugano, S.; Tanabe, Y.; Kamimura, H. *Multiplets of Transition-Metal Ions in Crystals*; Academic Press: New York, NY, USA, 1970.
123. Carlotto, S.; Sambi, M.; Vittadini, A.; Casarin, M. Mn(acac)$_2$ and Mn(acac)$_3$ complexes, a theoretical modelling of their $L_{2,3}$-edges X-ray absorption spectra. *Polyhedron* **2017**, *135*, 216–223. [CrossRef]
124. Simonov, K.A.; Vinogradov, A.S.; Brzhezinskaya, M.M.; Preobrajenski, A.B.; Generalov, A.V.; Yu Klyushin, A. Features of metal atom 2p excitations and electronic structure of 3d-metal phthalocyanines studied by X-ray absorption and resonant photoemission. *Appl. Surf. Sci.* **2013**, *267*, 132–135. [CrossRef]
125. Bartolomé, J.; Bartolomé, F.; Brookes, N.B.; Sedona, F.; Basagni, A.; Forrer, D.; Sambi, M. Reversible Fe Magnetic Moment Switching in Catalytic Oxygen Reduction Reaction of Fe-Phthalocyanine Adsorbed on Ag(110). *J. Phys. Chem. C* **2015**, *119*, 12488–12495. [CrossRef]
126. Betti, M.G.; Gargiani, P.; Frisenda, R.; Biagi, R.; Cossaro, A.; Verdini, A.; Floreano, L.; Mariani, C. Localized and Dispersive Electronic States at Ordered FePc and CoPc Chains on Au(110). *J. Phys. Chem. C* **2010**, *114*, 21638–21644. [CrossRef]
127. Stepanow, S.; Lodi Rizzini, A.; Krull, C.; Kavich, J.; Cezar, J.C.; Yakhou-Harris, F.; Sheverdyaeva, P.M.; Moras, P.; Carbone, C.; Ceballos, G.; et al. Spin Tuning of Electron-Doped Metal–Phthalocyanine Layers. *J. Am. Chem. Soc.* **2014**, *136*, 5451–5459. [CrossRef]